Beta decay of $^{100}_{40}$Zr produced in neutron-induced fission of natural uranium

Thokozani Kamoto

Supervisor: Prof. D. G. Roux

Thesis submitted to Rhodes University in fulfilment of the requirements for the degree of Master of Science

Department of Physics and Electronics

Rhodes University

South Africa

March 07, 2016

Abstract

Fission fragments, produced by neutron bombardment of natural uranium at the Physics Department, Jyväskylä, Finland, are studied in this work. The data had been sorted into 25 $\gamma - \gamma$ coincidence matrices which were then analysed. In this work we aimed to identify the fission products using γ-γ coincidence analysis and then study the beta-decay of some of the fission products. Sixteen fission products ranging from A = 94 to A = 136 were identified. Out of these fission products beta decay of the A = 100 ($^{100}_{40}$Zr - $^{100}_{41}$Nb - $^{100}_{42}$Mo) chain was studied in greater detail. We have also studied the variation of the relative intensities as a function of time of the 159-, 528-, 600-, 768-, 928- and 1502-keV γ-ray lines in $^{100}_{42}$Mo and the profiles of the relative intensities have been modelled with the variation of the activity of $^{100}_{41}$Nb against time. Configuration assignments of ^{100}Zr and $^{100}_{42}$Mo are discussed.

Acknowledgements

I would like to thank my supervisor, Prof. David G. Roux, for the support rendered to me in the course of developing this research work. That is, he was readily available to assist me whenever I required guidance. I would like to also thank the head of the Department of Physics and Electronics at Rhodes University, Prof. Makaiko Chithambo, for the support I received from the Department throughout my study period. Further, I thank the management of Mzuzu University for facilitating the funding process of my study by the African Development Bank. Finally, I say thank you to my family in Malawi for your endless support.

Contents

List of Figures

List of Tables

Chapter 1

Introduction

Nuclear physicists aim to study properties of nuclei through experiments and theoretical models. Among the quantities of interest are the excitation energies, spins, configurations and modes of decay. The choice of which experiment to perform is usually guided by the predictions of the theoretical models. Nuclei can be produced via the neutron-induced fission reaction. This kind of reaction produces radioactive nuclides which facilitate beta-decay and nuclear-structure studies. Neutron-induced fission reactions of uranium were studied in previous works [1, 2]. In those works the measurements were taken 60 seconds [1] and at least 1 hour [2] after irradiation. Short-lived fission products might have escaped measurement in the previous works. Recently, however, a neutron-induced fission reaction of natural uranium was studied in which case the time delay between the end of irradiation and commencement of measurement was only 1.2 seconds [3]. With this short time delay it was hoped that short-lived fission products could be found. The present work, therefore, is aimed at identifying the fission products using γ-γ coincidence analysis. Furthermore, the beta decay of A = 100 chain radionuclides was studied. This chain was chosen due to the ambiguity that arises from the population of $^{100}_{42}$Mo by $^{100}_{41}$Nb in that there are two possible states of $^{100}_{41}$Nb, namely

the 1^+ ground state [4] and the (4^+, 5^+) isomeric state [5], which can populate $^{100}_{42}$Mo hence the need for an investigation of the population of energy levels of $^{100}_{42}$Mo. Furthermore, we have investigated the variation of the relative intensity as a function of time of the 159-, 528-, 600-, 768-, 928-keV and 1502-keV gamma-ray lines associated with de-excitation of the $^{100}_{42}$Mo nucleus. Lastly, configuration assignments of the ground state of $^{100}_{40}$Zr and $^{100}_{42}$Mo are discussed based on the previous works.

This work has been organized as follows: Chapter 2 describes a brief history of neutron-induced fission and the theoretical models. Chapter 3 describes the experimental techniques for detection of γ rays. Chapter 4 is about the experiment and the process of data analysis. Chapter 5, which is the main part of this thesis, presents the partial level schemes and the gated spectra for the identified fission products, a discussion of beta decay of the A = 100 ($^{100}_{40}$Zr - $^{100}_{41}$Nb - $^{100}_{42}$Mo) chain, the obtained plots of the relative intensities against time of six γ-ray lines in $^{100}_{42}$Mo, and a study of configuration assignments in ^{100}Zr and $^{100}_{42}$Mo. Chapter 6 presents a summary of the study and a discussion of possible future work.

Chapter 2

Theory

2.1 Nuclear fission processes

2.1.1 Discovery of neutron-induced fission

The discovery of radioactivity by Antoine Henri Becquerel in early 1896 [6] and neutrons by James Chadwick in 1932 [7] encouraged several nuclear physicists to find out what could happen if some radioactive elements were bombarded with neutrons. With the hope of producing new elements with greater atomic mass than that of uranium in 1938, Otto Hahn and Fritz Strassmann [8] irradiated uranium with neutrons (Appendix A). To their great surprise uranium was not producing new heavy elements, rather it was energetically splitting into lighter elements which they had already known. In their attempt to provide an explanation of this new phenomenon Meitner and Frisch [9] suggested that it was similar to the splitting of a vibrating liquid drop into two smaller drops. Consequently, they proposed the term "fission" which was analogous to the division of the biological cells.

The liquid drop model is used to describe the macroscopic behaviours of a nucleus. Nuclear fission is an example of a macroscopic behaviour explained using this model. Here,

a nucleus is regarded as an electrically charged drop which gains excess energy by absorbing a neutron, resulting in violent oscillations. These oscillations cause a neck between two lobes to form (see Figure 2.1). The repulsive force between the lobes widens the neck farther thereby leading to the formation of two smaller drops. This happens when the excitation energy gained by the splitting nucleus is greater than the potential barrier.

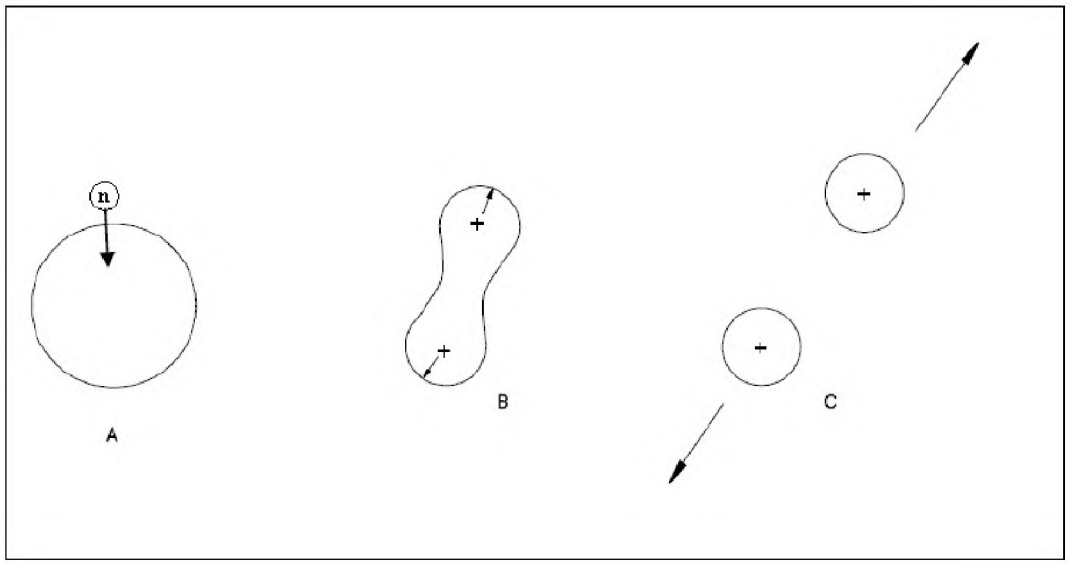

Figure 2.1: Mechanism of nuclear fission as per the liquid drop model |10|.

2.2 Beta decay

Beta decay is a radioactive decay process which involves conversion of either a neutron to a proton or a proton to a neutron, leading to changes in both the number of protons (Z) and neutrons (N) of the atomic nucleus. However, the mass number (A = Z + N) does not change. There are three beta-decay processes, namely negative beta decay (β^-), positive beta decay (β^+) and orbital electron capture (ε). During β^- decay only the neutron is transformed to proton thereby increasing Z and decreasing N. This process is given by |11|:

$$n \longrightarrow p + e^- + \tilde{\nu}_e, \tag{2.1}$$

where $\tilde{\nu}_e$ is the antineutrino and e^- is an electron. In β^+ decay the proton is converted to a neutron resulting in an increase in N and a decrease in Z. This is described as [11],

$$n \longrightarrow p + e^+ + \nu_e. \tag{2.2}$$

In this case, e^+ and ν_e are the positron and neutrino respectively. The orbital electron capture involves the capture of an atomic electron. This process takes place only for protons which are bound in a nucleus.

2.2.1 Beta decay selection rules

Depending on the total orbital angular momentum, l, taken away by the electron (or positron) and antineutrino (or neutrino) beta decay can be classified as allowed or forbidden. For allowed case the orbital angular momentum is zero whereas for forbidden beta decay the orbital angular is greater or equal to 1 ($l \geq 1$). Moreover, if $l = 1$ and $l = 2$ beta decay transitions are known as first forbidden and second forbidden transitions respectively. The parity, π, of the beta-decay transition is given by [12]:

$$\pi = (-1)^l . \tag{2.3}$$

Thus, we expect a parity change for $l = 1$ while no change in parity is expected for $l = 2$. Beta decay can be further classified as Fermi decay or Gamow Teller decay. The electron (positron) and antineutrino (neutrino) have an intrinsic $\frac{1}{2}$ spin. When these two spins are oriented in the opposite directions they cancel out and this is called Fermi decay. If the half-integer spins are oriented in the same directions the decay is called Gamow Teller decay. The selection rules for beta decay are listed in Table 2.1.

Table 2.1: Beta decay selection rules and $\log ft$ values [13].

Type of transition	log ft	L	Fermi		Gamow-Teller	
			ΔI	$\Delta\pi$	ΔI	$\Delta\pi$
Allowed	<5.9	0	0	no	0,1	no
First forbidden	>6.0	1	0,1	yes	0,1,2	yes
Second forbidden	>10.6	2	1,2	no	2,3	no

2.2.2 Log ft values

The comparative half life is expressed as a product of the Fermi integral function $f(Z,Q)$ and the beta decay half life $t_{1/2}$. Thus:

$$ft_{1/2} = f(Z,Q)\, t_{1/2} \tag{2.4}$$

The decay constant is related to the Fermi integral function by [12]:

$$\lambda = \frac{m_e^5 c^4}{2\pi^3 \hbar^7} g^2 \left|M_{if}\right|^2 (Z,Q)\,. \tag{2.5}$$

By making use of the relationship,

$$t_{1/2} = \frac{\ln(2)}{\lambda}, \tag{2.6}$$

the comparative half life in equation 2.4 can be written as:

$$ft_{1/2} = \frac{1.386\pi^3\hbar^7}{m_e^5 c^4} \ln(2) \frac{1}{g^2 \left|M_{if}\right|^2}, \tag{2.7}$$

where g^2 is the square of the strength of weak interaction, $|M_{if}|^2$ is the square of the nuclear matrix element. It can be seen in Equation 2.7 that the comparative half life is inversely proportional to the square of the nuclear matrix element. It turns out, therefore, that the

greater the value of $|M_{if}|^2$ the more probable the transition and the smaller the value the less probable the transition. Further, the lowest value of $ft_{1/2}$ is reached when $|M_{if}|^2$ tends to unity, and this corresponds to superallowed transitions. Because of the large range of beta decay half-lives the $\log_{10} ft_{1/2}$ is used instead of $ft_{1/2}$.

2.3 The Nilsson model

It is known that the shell model only becomes useful when describing nuclei which are spherical or have closed shells. However, most nuclei are deformed. In his attempt to come up with a potential for the deformed nuclei Sven G. Nilsson, in 1955, formulated the Nilsson model. In this model the deformed single-particle Hamiltonian $\hat{H}_{sp}$ is expressed as follows [14]:

$$\hat{H}_{sp} = \frac{\hat{p}^2}{2M} + V_{\text{Nilsson}}, \tag{2.8}$$

with

$$V_{\text{Nilsson}} = V_h - C\hat{s} \cdot \hat{l} - D\hat{l}^2. \tag{2.9}$$

Here V_{Nilsson} is the deformed Nilsson potential, V_h is the harmonic oscillator potential, $C\hat{s} \cdot \hat{l}$ and $D\hat{l}^2$ represent the spin-orbit interaction and reproduce the splitting between energy levels for different values of angular momentum (l). The single-particle orbitals associated with the deformed potential are described by the Nilsson quantum numbers:

$$\Omega^{\pi} \left[N, n_z, \Lambda\right], \tag{2.10}$$

where Ω is the projection of the single-particle angular momentum (that is , $\Omega = \Lambda \pm \frac{1}{2}$), N is the principal quantum number of the major shell, Λ and Σ denote the projection of orbital momentum (l) and spin (s) on the symmetric axis respectively. This is illustrated in Figure 2.2.

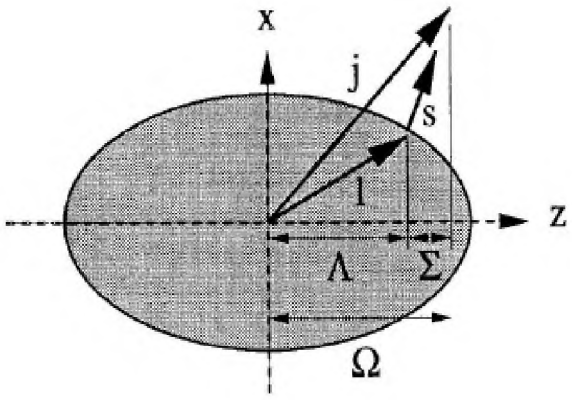

Figure 2.2: Schematic diagram for the Nilsson quantum numbers [15].

As an example, the Nilsson's diagrams for the single-particle energy levels as a function of the Nilsson's deformation parameter ε_2 for the protons in the $50 \leqslant Z \leqslant 82$ region and neutrons in the $50 \leqslant N \leqslant 82$ region are shown in Figures 2.3 and 2.4 respectively. The Nilsson's deformation parameter ε_2 used in these diagrams is related to the quadrupole deformation parameter β_2 as [16]:

$$\varepsilon_2 \approx 0.944\beta_2 - 0.122\beta_2^2. \tag{2.11}$$

Prolate-shaped nuclei have positive values of the deformation parameters while oblate-shaped nuclei have negative values.

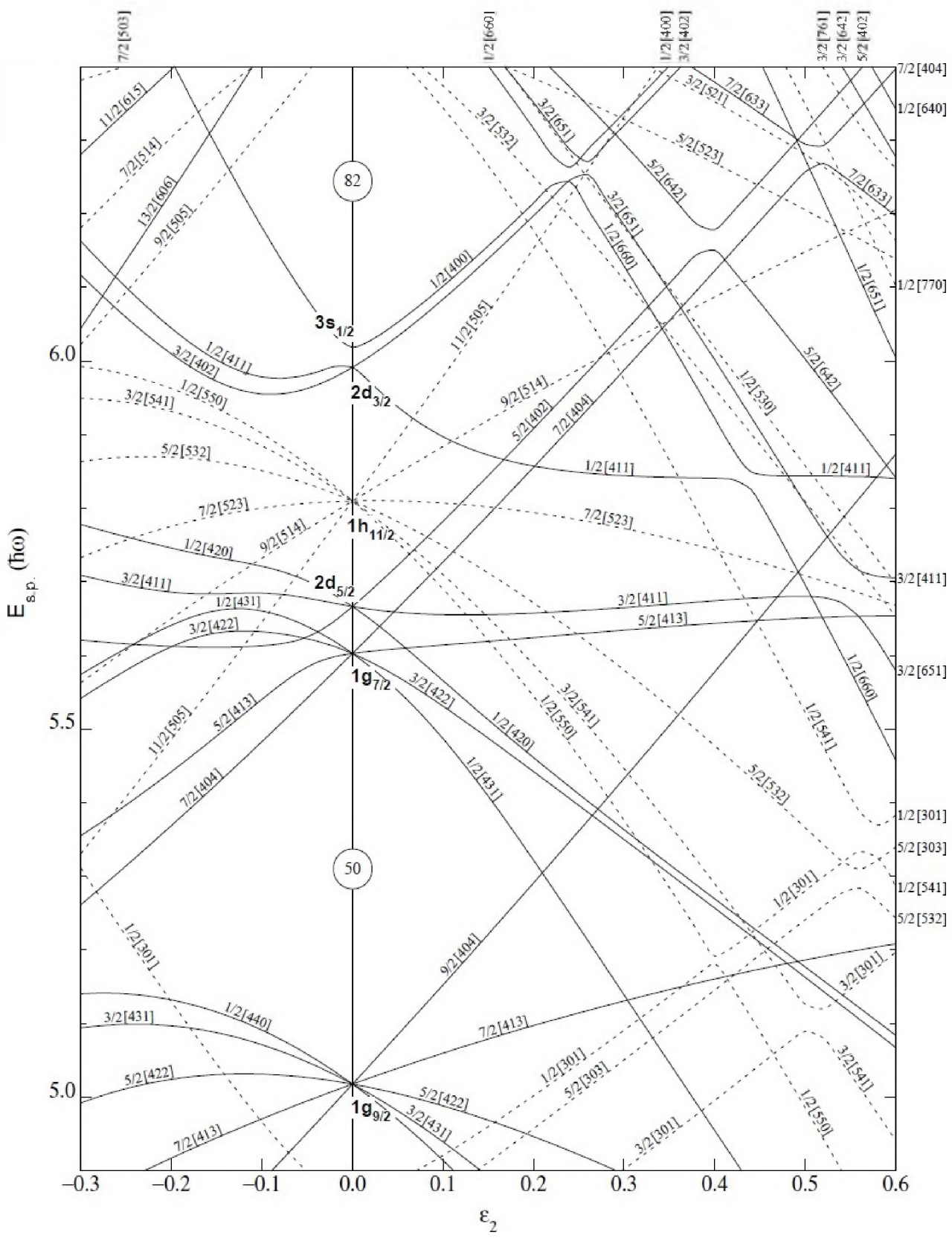

Figure 2.3: Nilsson diagram for protons, $50 \leq Z \leq 82$ ($\varepsilon_4 = \varepsilon_2^2/6$) [17].

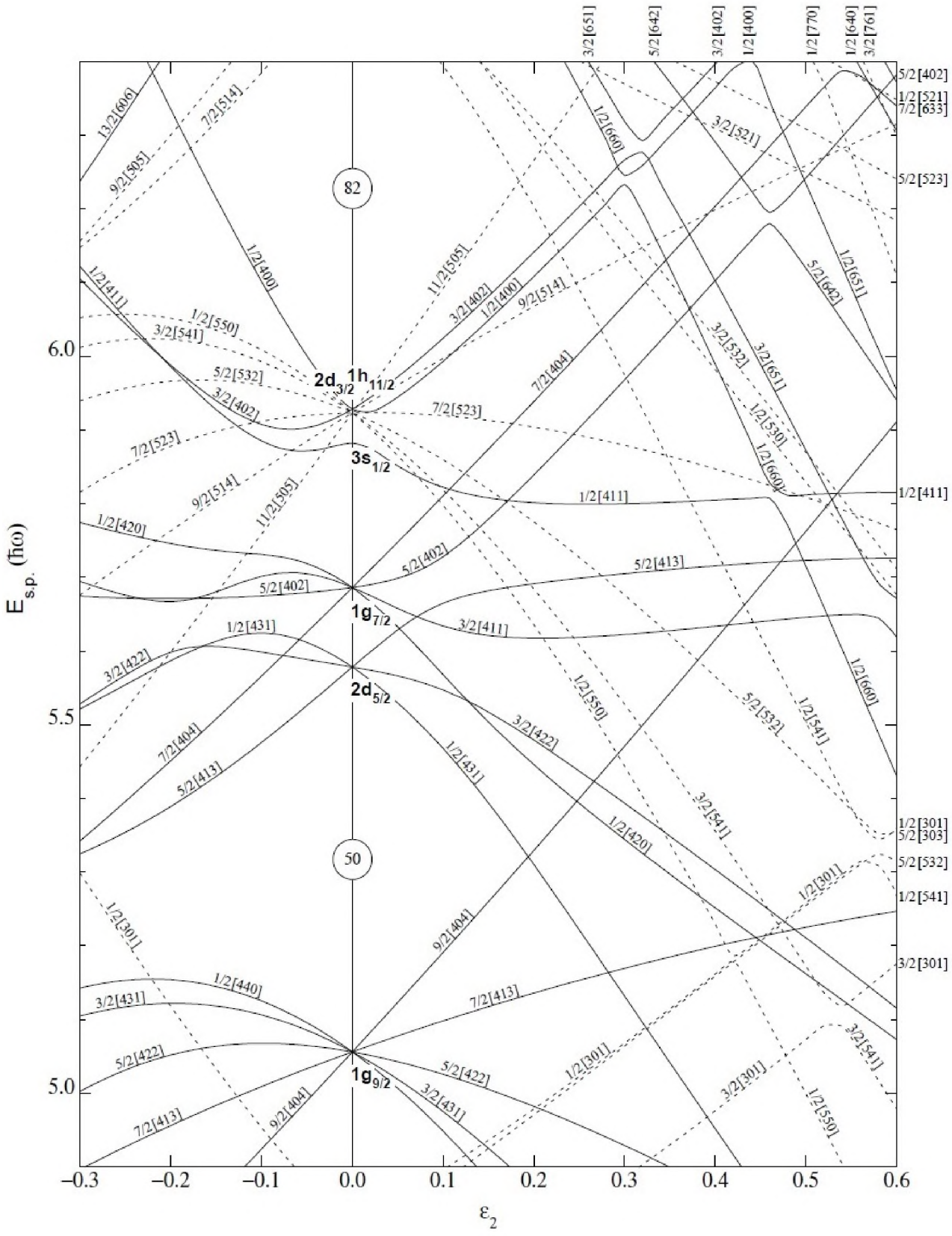

Figure 2.4: Nilsson diagram for neutrons, $50 \leq N \leq 82$ ($\varepsilon_4 = \varepsilon_2^2/6$) [17].

Nuclear shapes can be expressed in terms of the spherical harmonics by expanding the vector radius from the origin to the nuclear surface, and the length of a radius vector R(θ, ϕ) is given by [18]:

$$R(\theta, \phi) = R_0 \left[1 + \sum_{\lambda=0}^{\infty} \sum_{\mu=-\lambda}^{\lambda} \alpha_{\lambda\mu} Y_{\lambda\mu}(\theta, \phi) \right], \tag{2.12}$$

where R_0 is the radius of the sphere with a uniform volume, θ and ϕ are polar angles related to the arbitrary set of coordinates. Under the volume conservation requirement, λ and μ are both equal zero. The deformation parameter $\alpha_{00} = 0$ is consistent with an interpretation of the spherical shape. For α_{20} ($\lambda = 2$, $\mu = 0$) and α_{22} ($\lambda = 2$, $\mu = 2$) the physical system is represented by two variables β_2 and γ as follows:

$$\alpha_{20} = \beta_2 \cos\gamma, \tag{2.13}$$

and

$$\alpha_{22} = \beta_2 \frac{1}{\sqrt{2}} \sin\gamma. \tag{2.14}$$

Here, β_2 is the quadrupole deformation parameter that measures the deviation of the nuclear shape from the spherical shape, γ is the triaxiality parameter. The larger the value of β_2 the more deformed the nucleus becomes (refer to Figure 2.5).

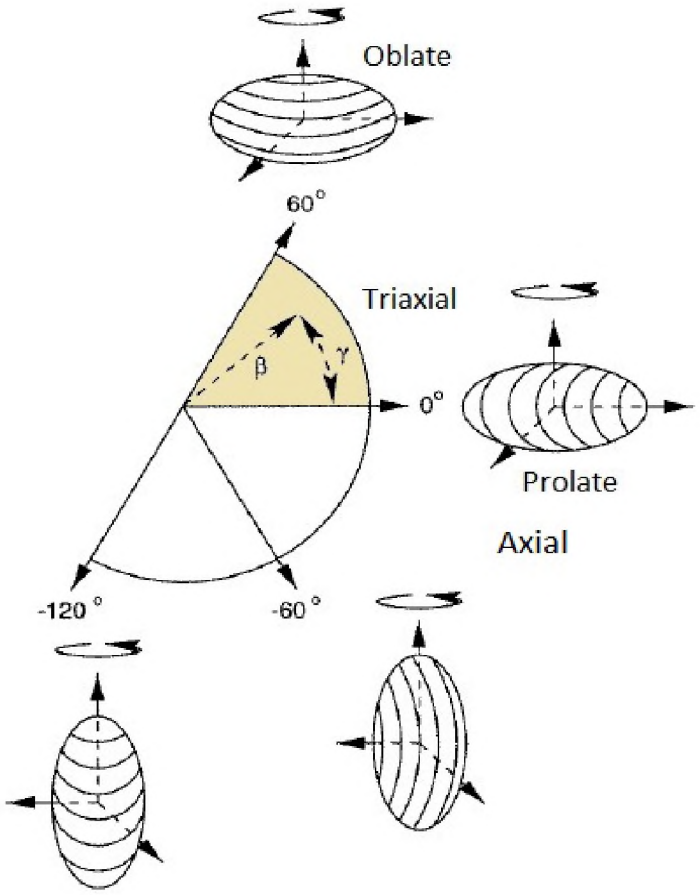

Figure 2.5: Nuclear shape parametrisation. $\gamma = 0°$ and $\gamma = -60°$ describe axially-symmetric prolate and oblate shapes respectively. $\gamma = -120°$ and $\gamma = 60°$ describe the triaxial prolate and oblate shapes respectively. The circular arrows indicate the rotation axes |15|.

Chapter 3

Experimental techniques

3.1 Gamma-ray interaction with matter

γ rays are detected when they interact with a detector [19]. It is for this reason that the γ-ray interaction processes with matter; photoelectric, Compton scattering and pair production are discussed in this section.

The photoelectric process involves interaction of the γ ray with a bound atomic electron in which case all the energy of the γ ray is lost such that the γ ray ceases from existing [20]. This process is described by the following equation [21]:

$$E_e = E_\gamma - E_b \,, \tag{3.1}$$

where E_e is the kinetic energy gained by an electron, E_γ the energy of the γ ray and E_b is the binding energy of the electron in the K or L shells of an atom. The probability (τ) of photoelectric absorption increases with an increase in the atomic number (Z)[22]:

$$\tau \;\propto\; Z^5 \,. \tag{3.2}$$

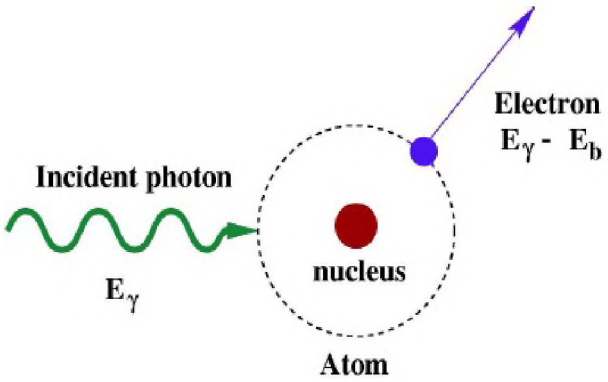

Figure 3.1: The mechanism for photoelectric absorption [23].

Compton scattering involves a direct interaction between a γ ray and a weakly bound electron. This process takes place within the energy range 150 keV - 1800 keV. The kinetic energy of the recoiling electron (E_e) and the γ- ray energy (E_γ) are described as [24]

$$E_e = E_\gamma \left[1 - \frac{1}{1 + E_\gamma \left(1 - \cos\theta\right) / m_0 c^2}\right], \tag{3.3}$$

where θ is the angle between the scattered photon and the direction of the incident photon, and m_0c^2 is the rest mass of the electron. For any value of the angle θ, E_e is less than E_γ. The maximum energy transferred to the electron, called the Compton edge, occurs if the γ ray scatters in the opposite direction (that is, when $\theta = 180°$, see Figure 3.2). No energy is transferred to the detector when the γ ray scatters in forward direction (that is, for $\theta = 0°$).

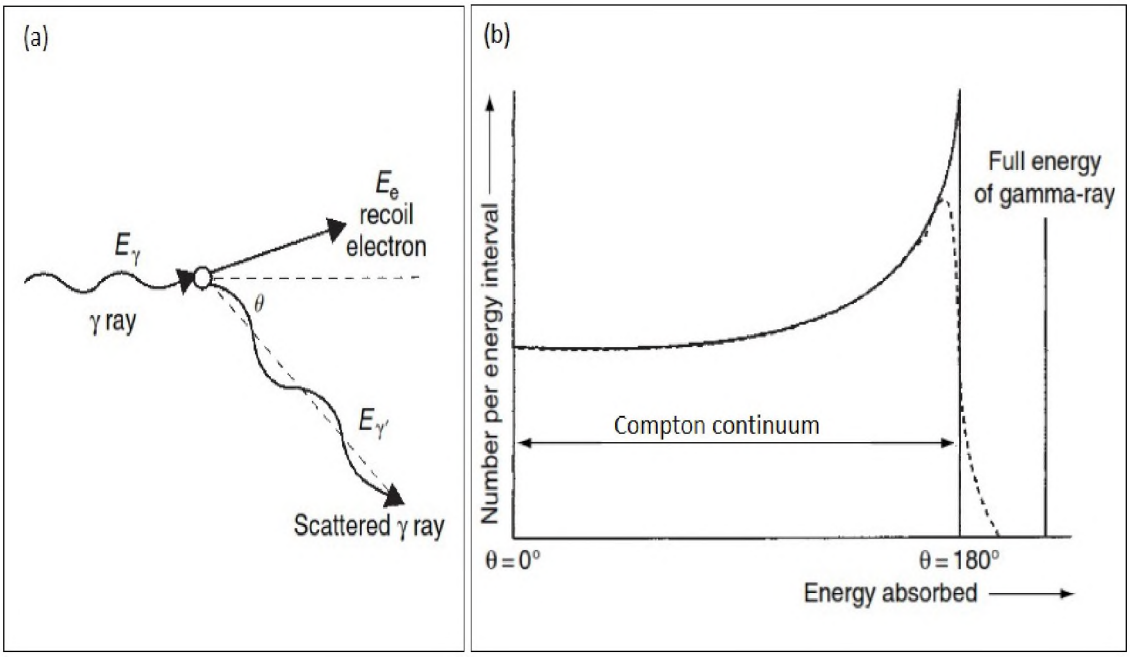

Figure 3.2: Panel (a) shows Compton scattering mechanism whereas Panel (b) shows how the energy transferred to the absorber by Compton scattering varies as a function of the scattering angle |19|.

Unlike the photoelectric absorption and Compton scattering processes, the pair-production process describes an interaction of the γ ray with an atom as a whole under the influence of the strong electromagnetic field thereby creating an electron-positron pair. This process takes place when the threshold energy is 1022 keV (that is, $E_\gamma \geq 1022$ keV). The positron formed through this process, after losing its energy, is immediately converted to photons when it combines with an electron via the annihilation process (refer to Figure 3.3). The 511-keV annihilation γ ray if absorbed by the detector appears in the energy spectrum.

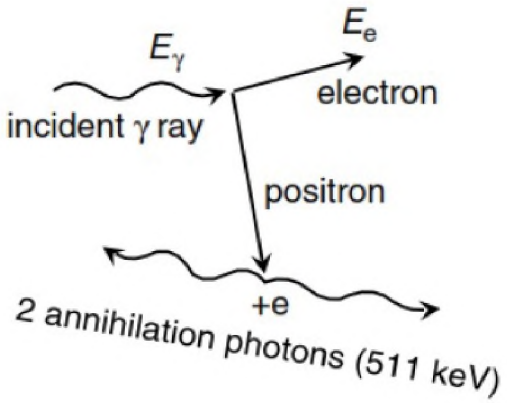

Figure 3.3: Pair production mechanism |19|.

3.2 The semiconductor γ-ray detector

Various semiconductors are used to detect γ rays. Some of the semiconductor materials used include germanium and silicon. In the experiment that led to the production of the present work high-purity germanium (HPGe) detectors were used. This section, therefore, focuses on the discussion of semiconductors and HPGe detectors.

Semiconductors can be regarded as being materials whose electrical conductivity lies between that of insulators and conductors. They have a valence band which contains free electrons and an empty-conduction band. These two bands are separated by a band gap as shown in Figure 3.4. Conduction takes place when an electron in the valence band gains enough energy to pass through the energy gap (1 eV) and enters into the conduction band. This electron leaves a hole in an atom which is filled by an electron from a nearby atom in the semiconductor material.

Electrical conduction in semiconductors is controlled by adding small amounts of dopants from either boron or phosphorus (refer to Figure 3.5). If a germanium semiconductor is doped with phosphorus all four valence electrons of germanium will contribute in the formation of

four covalent bonds, with only four out of five valence electrons of phosphorus. An excess electron is, therefore, introduced in the lattice and forms discrete donor states just below the conduction band. This semiconductor material is called n-type material because the majority charge carriers are negative charges (electrons). When a semiconductor is doped with boron an excess hole is produced and this introduces acceptor states above the valence band. For the reason that the majority charge carriers are holes (which are regarded as positive charges), this semiconductor is known as p-type material. Through the doping process the energy gap of a semiconductor is narrowed thereby increasing conductivity.

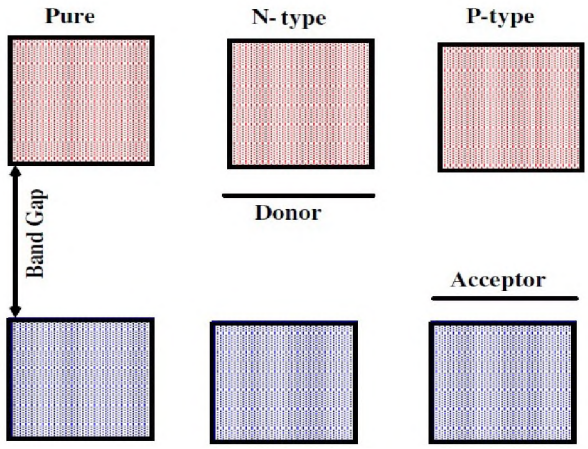

Figure 3.4: Semiconductor |22|.

When the n-type and p-type materials are joined the electrons in the n-type material migrate to the p-type material to fill the holes. The charge carriers are neutralized in the region around the p-n junction hence forming a region called depletion region. The positive and negative space charges are formed in the n-type and p-type sides respectively, leading to the formation of a potential barrier. The depletion region is an active element of a detector [19] for it interacts with incident γ rays and produce high energy photons which redistribute to form a pattern of electron-hole pairs, with electrons moving in one direction and holes flowing to the opposite direction. Under the influence of an electric field the collected electrons form an electrical pulse whose amplitude becomes proportional to the

energy lost by the incident γ ray. The depletion region can be increased by connecting the p-type and n-type sides to the negative and positive terminals of the power supply respectively. This is called reverse biasing.

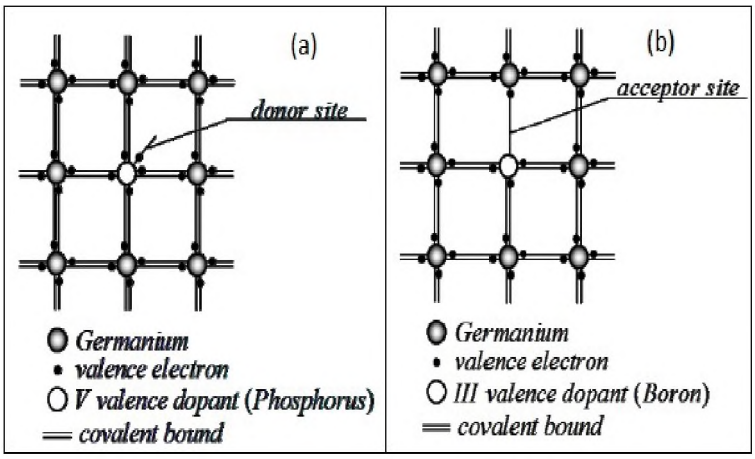

Figure 3.5: Doping process [19].

We now turn to HPGe detectors. These detectors have high resolution. Moreover, they have lower impurity level ($10^9/\text{cm}^3$) than that ($10^{12}/\text{cm}^3$) of other common detector materials [22]. As opposed to silicon detectors, germanium detectors can also operate under a high reverse bias voltage of up to 4 kV.

Compton scattering tends to cause a large Compton continuum for not all the γ-ray energy is transferred to the detector (see Figure 3.2). This results in difficulties to identify the low-intensity peaks and also increases the uncertainty of the measured activities. A technique known as Compton suppression is used to reduce background by preventing registration of the γ rays scattered from the detectors (see Figure 3.6). This is achieved by surrounding the HPGe detectors with scintillator detectors (using for example bismuth germinate (BGO) crystals).

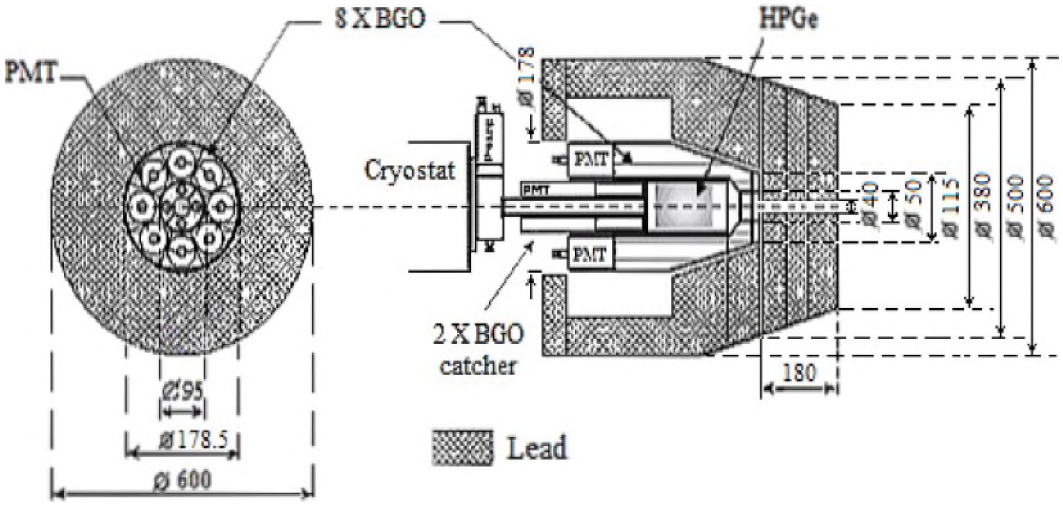

Figure 3.6: An example of a detector configuration allowing for Compton suppression |25|.

Chapter 4

Experiment and data analysis

4.1 Experiment

In an experiment on which the present work is based, fission products were produced when neutrons impinged the natural uranium metal disk of 12 mm diameter. Neutrons were produced through the d + ^{12}C reaction at a deuteron-beam energy of 40 MeV (refer to Figure 4.2) which was supplied by the K = 130 cyclotron at the Department of Physics, Jyväskylä, Finland [3]. The neutron spectrum (see Figure 4.2) was measured by activation of Al, Ni, In, and Bi foils. γ rays emitted from the high-spin states of the fission products were counted by the two high-purity germanium (HPGe) detectors (complete with their Compton suppression shields [3]) were placed at a distance of 12 cm from the center of the uranium target. In this fission experiment the measurements were performed as a succession of identical cycles. There were 1300 cycles consisting of 5 s irradiation, 1.2 s target transportation, and 25 s counting. It took 196 s to complete a cycle of irradiating 6 targets at the end of which, a given target was re-irradiated (see Figure 4.3 and Figure 4.4).

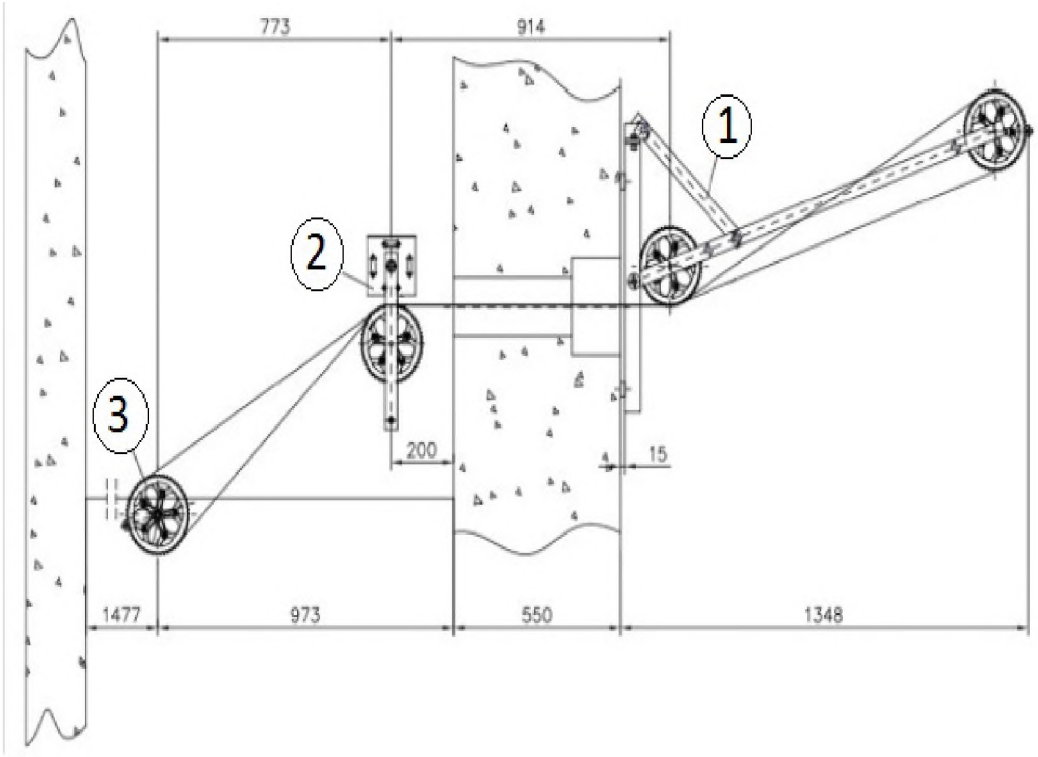

Figure 4.1: A side view of the bicycle chain-based transport system |3|: (1)upper swing, (2)lower swing, (3)driving wheel connected to the stepping motor. The labelled dimensions are in mm. Two out of the six target holders on chain are shown. The irradiated target disk is above the top of the upper wheel while the counted target is at the bottom of the wheel connected to the motor. HPGe detectors are looking in and out of the plane of the figure.

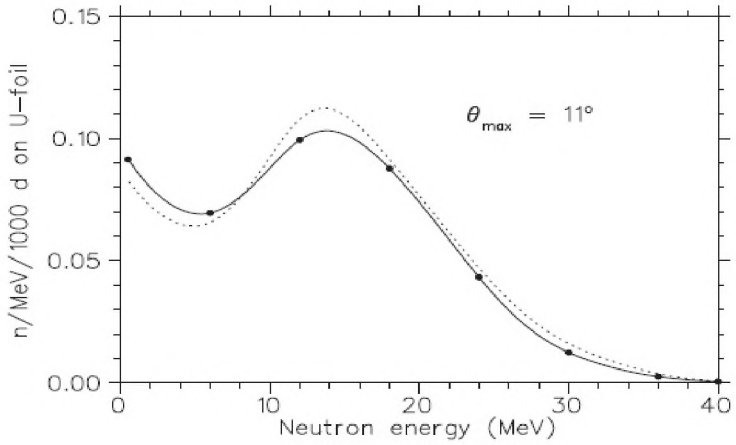

Figure 4.2: Neutron spectrum irradiating uranium disk [3]. 11° is the maximum emission angle of neutrons with respect to the beam axis. The dotted curve is the predicted spectrum.

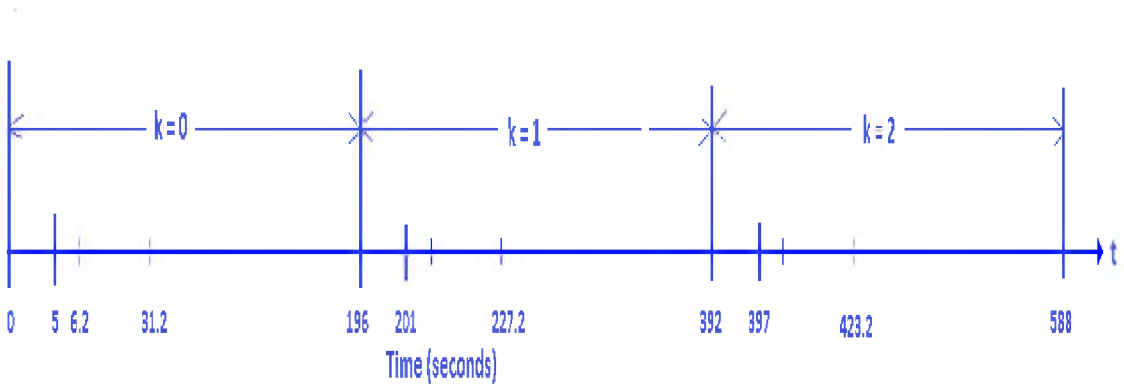

Figure 4.3: A diagrammatic representation of the proceedings of the experiment. For k = 0 case: $0s < t \leq 5s$ is the bombardment (beam-on) time-interval, $5s < t \leq 6.2s$ is the time interval the sample is moved to measurement position, $6.2s < t \leq 31.2s$ is the measurement time-interval. $31.2s < t \leq 196s$ is the time-interval the sample is transferred back to the bombardment region.

4.2 Data acquisition system

Preamplified-analog signals were digitized by a VHS-ADC digital signal processing (DSP) system|3|. The direction of flow of signals in a controller are indicated in Figure 4.4. More details about the data-acquisition process can be obtained from |3|.

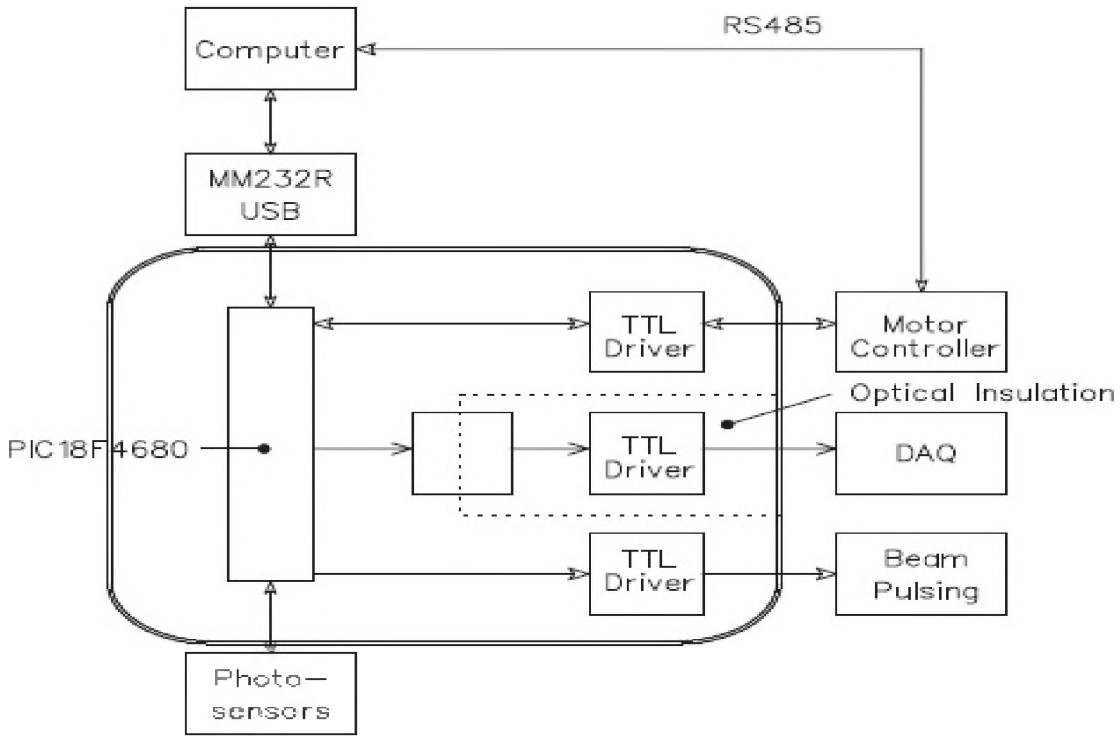

Figure 4.4: Schematic view of the controller [3]. The directions of signals are indicated by arrow heads.

4.3 Data analysis

4.3.1 Detector-efficiency calibration

The probability that the emitted γ ray interacts with the detector is known as detector efficiency. The relative efficiency of a detector depends on the geometry of the detector and the γ-ray energy deposited on the detector.

^{152}Eu and ^{60}Co standard calibration sources [3] were used to perform efficiency measurements of the the HPGe detectors at the Physics Department, Jyväskylä, Finland. Figure 4.5 shows how the normalized-relative efficiency of the present-experimental work varies with the γ-ray energy. The maximum relative efficiency was reached at an energy value of about 200 keV. The efficiency parameterization was deduced from the curve shown in Figure 4.5.

Gf3 program was used to set the Radware background. The matrix file was read in gf3

and the bg command was used to set the background in which case a length factor of 1.0 was chosen. The background was then saved as a new .spe file. The escl8r program required the background .spe file to create the .esc file from the .mat file.

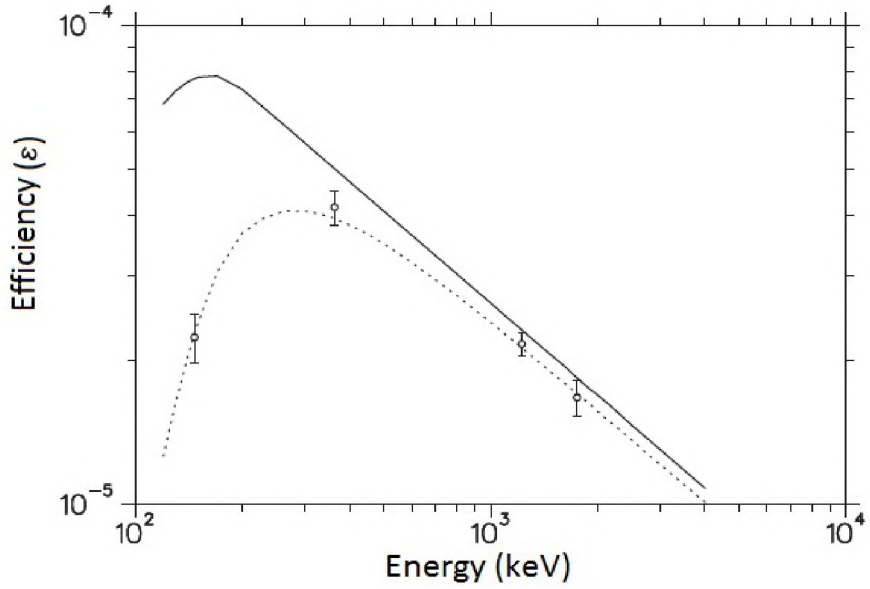

Figure 4.5: The efficiency of HPGe detectors as a function of γ-ray energy [3]. A fit of efficiency for pairs (906 keV, E_γ) emitted by a point source is given by the solid line. The dashed line is the corrected-efficiency curve. The detection efficiency is relative.

4.3.2 γ-γ coincidence analysis

γ-γ coincidence events for the energies of the detected γ rays were stored in a two-dimensional histogram known as a matrix, with a dimension of 4096 $\times$ 4096 channels. RadWare [26] was used for data analysis. *Escl8r* and $gf3$ programs of this software were mainly used. In the fission experiment there were 13000 cycles and each cycle consisted of, apart from other events, 25 seconds for counting. The first matrix represented an average of 1 second for counting, the second matrix represented an average of 2 seconds for counting and so on. Twenty-five matrices represented the measurement time of twenty-five seconds. These matrices were obtained from the Physics Department, Jyväskylä, Finland. The first 24 matrices were combined pairwise to produce 12 matrices with enhanced statistics. The 25th

matrix was discarded.

In the present study the process of assigning spins and parities was not possible because of the limitation in data. The experimental set up did not include angular distribution and anisotropy measurements. For this reason, spins and parities of the identified fission products were adopted from the previous works |27, 28, 29, 30, 4, 31, 32, 33, 34, 35|.

4.3.3 Identification of fission products

In order to identify fission products a process known as gating is performed. This process involves setting a gate around a gamma-ray peak of interest in the gamma-gamma matrix using the *escl8r* program and then projecting all the gamma-rays in coincidence into a one-dimensional spectrum. An example of a simple level scheme is shown in Figure 4.6. If a gate is set on the E_2 transition the γ with energy E_1 will be seen in the spectrum because it is in coincidence with the E_2 transition. However, the γ ray with the energy E_3 will not be seen in the spectrum because it is not in coincidence with the gating transition (E_2). In this way, γ rays can be located and confirmed in the level scheme.

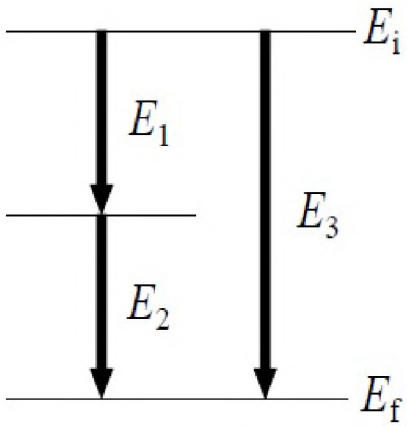

Figure 4.6: A schematic diagram of energy for construction of a level scheme |36|.

Chapter 5

Results and discussion

This chapter presents the tabulated information, gated spectra and partial level schemes of the identified fission products. A beta-decay study of the A = 100 ($^{100}_{40}$Zr - $^{100}_{41}$Nb - $^{100}_{42}$Mo) chain is also presented. Moreover the plots of the relative intensities as a function of time of six γ-ray lines in $^{100}_{42}$Mo are discussed. Furthermore the configuration assignments in $^{100}_{42}$Mo and $^{100}_{40}$Zr are discussed.

5.1 Identified fission products

The first aim of the present work was to identify the fission products using γ-γ coincidence analysis. Sixteen nuclides ranging from A = 94 to A = 136 were found (see Table 5.1). The initial and final excitation energies, and the initial and final parities for the identified fission products are listed in Tables 5.2 and 5.3. Transitions which were used as gates of the identified fission products are shown in Figure 5.1. For instance, Figure 5.1 (c) shows the 836-keV, $2^+ \longrightarrow^+ 0^+$ ground-state transition which has been used as a gate to pick out gamma-rays associated with $^{94}_{38}$Sr decay. The gated spectra and partial level schemes of the fission products are juxtaposed in Figures 5.2, 5.3, 5.4, 5.5, 5.6 and 5.7. These figures were

obtained from the first γ-γ matrix. This γ-γ matrix was chosen because it contained short-lived fission products. As an example, Figure 5.2 shows the known level scheme of $^{94}_{38}$Sr on the right (d), and the spectrum observed when a gate is set on the 836-keV ground-state transition, on the left (a). In this spectrum one can see strong γ-ray peaks at 1309, 1577 and 1089 keV. These γ rays are known to be in coincidence with the gate in the nuclide $^{94}_{38}$Sr. We can therefore be certain that $^{94}_{38}$Sr occurs in our data. Also present in this Figure 5.2 are the level scheme, to the right (e) and spectrum, to the left (b) obtained by setting a gate on the 122-keV ground-state transition of $^{96}_{39}$Y. The 809-keV transition which is in coincidence with the 122-keV gate is strongly observed. This confirms the presence of $^{96}_{39}$Y in the present work. The other γ rays seen in this spectrum are the known contaminants. In the same Figure 5.2 ((c),(f)), six transitions are confirmed for $^{96}_{40}$Zr. When a gate is set on the 1750-keV transition, γ-ray peaks are strongly seen at 146, 363, 616, 914, 1106, and 1222 keV.

Table 5.1: Identified nuclides. The properties listed below have been adopted from [37], [38].

Gate (keV)	Nuclide	I^π for the ground state	Half life	Decay mode
836	$^{94}_{38}$Sr	0^+	75.3 s	β^-
122	$^{96}_{39}$Y	0^-	5.34 s	β^-
1750	$^{96}_{40}$Zr	0^+	2.35×10^{19} y	$2\beta^-$
620	$^{98}_{40}$Zr	0^+	30.7 s	β^-
213	$^{100}_{40}$Zr	0^+	7.1 s	β^-
104	$^{100}_{41}$Nb	1^+	1.5 s	β^-
104	$^{100}_{41}$Nb	$(4^+, 5^+)$	2.99 s	β^-
535	$^{100}_{42}$Mo	0^+	7.3×10^{18} y	$2\beta^-$
295	$^{102}_{42}$Mo	0^+	0.78×10^{19} y	β^-
192	$^{104}_{42}$ Mo	0^+	60 s	β^-
349	$^{112}_{46}$Pd	0^+	21.03 h	β^-
333	$^{114}_{46}$Pd	0^+	2.42 m	β^-
1279	$^{134}_{52}$Te	0^+	41.8 m	β^-
210	$^{134}_{53}$I	$(4)^+$	52.5 m	β^-
847	$^{134}_{54}$Xe	0^+	5.8×10^{22} y	$2\beta^-$
1132	$^{135}_{54}$Xe	$\frac{3}{2}^+$	9.14 h	β^-
1313	$^{136}_{54}$Xe	0^+	2.4×10^{21} y	$2\beta^-$

Table 5.2: γ-ray transitions of the identified nuclides populated through the neutron-induced fission of natural uranium. E_i and E_f are energies of initial and final energy levels of the γ ray, respectively. I_i^π and I_f^π are the initial and final spins (parities) [27, 28, 29, 30, 4, 38].

Nuclide	Gating transition (keV)	Coincident γ ray (keV)	E_i, E_f (keV)	$I_i^\pi \longrightarrow I_f^\pi$
$^{94}_{38}$Sr	836	504	2650, 2146	(4^+), (4^+)
	836	678	2604, 1926	(4^-), (3^-)
	836	813	2739, 1926	(4^-), (3^-)
	836	1089	1926, 837	(3^-), 2^+
	836	1309	2146, 837	4^+, 2^+
	836	1577	2414, 837	(3^-), 2^+
$^{96}_{39}$Y	122	530	652, 122	2^-, 0^-
	122	595	719, 122	unknown, 1^-
	122	809	932, 122	1^+, 1^-
	530	122	122, 0	1^-, 0^-
	530	276	932, 652	1^+, 2^-
	530	356	1288, 932	unknown, 1^+
$^{96}_{40}$Zr	1750	146	1897, 1750	3^-, 2^+
	1750	363	3483, 2857	6^+, 5^-
	1750	616	4390, 3772	8^+, 6^+
	1750	914	3772, 2857	6^+, 4^+
	1750	1106	2857, 1750	4^+, 2^+
	1750	1222	3119, 1897	5^-, 3^-
$^{98}_{40}$Zr	620	647	2190, 1543	6^+, 4^+
	620	769	3684, 2915	(10^+), 8^+
	620	1223	0, 1223	2^+, 0^+
	1223	620	1843, 1223	4^+, 2^+
$^{100}_{40}$Zr	213	352	565, 213	(4^+), 2^+
		498	1063, 565	(6^+), (4^+)
$^{100}_{41}$Nb	104	401	401, 0	(1^+), 1^+
$^{100}_{42}$Mo	535	159	695, 536	0^+, 2^+
	535	528	1064, 536	2^+, 2^+
	535	600	1136, 536	4^+, 2^+
	535	768	1464, 695	2^+, 0^+
	535	928	1464, 536	2^+, 2^+
	535	966	2103, 1136	4^-, 4^+
	535	1022	2085, 1064	0^+, 2^+
	535	1280	2416,1136	(4^+), 4^+
	535	1502	2038, 536	0^-, 2^+

Table 5.3: γ-ray transitions of the identified nuclides populated through the neutron-induced fission of natural uranium. E_i and E_f are energies of initial and final energy levels of the γ ray, respectively. I_i^π and I_f^π are the initial and final spins (parities) [31, 32, 33, 34, 35].

Nuclide	Gating transition(keV)	Coincident γ ray (keV)	E_i, E_f	$I_i^\pi \longrightarrow I_f^\pi$
$^{102}_{42}$Mo	295	401	696, 295	0^+, 2^+
	295	446	742, 295	4^+, 2^+
	295	551	847, 295	2^+, 2^+
	295	655	1397, 742	4^+, 4^+
$^{104}_{42}$Mo	192	368	560, 192	4^+, 2^+
	192	620	812, 192	2^+, 2^+
	192	772	1583, 812	4^+, 2^+
	192	836	1028, 192	3^+, 2^+
$^{112}_{46}$Pd	349	213	1096, 883	3^+, 4^+
	349	359	1096, 737	3^+, 2^+
	349	388	737, 349	2^+, 2^+
	349	534	883, 349	4^+, 2^+
	349	747	1096, 349	3^+, 2^+
$^{114}_{46}$Pd	333	317	1012, 695	3^+, 2^+
	333	362	695, 333	2^+, 2^+
	333	519	852, 333	4^+, 2^+
	333	620	1631, 1012	5^+, 3^+
	333	647	1501, 852	5^+, 4^+
	333	680	1012, 333	3^+, 2^+
$^{134}_{52}$Te	1279	297	1596, 1279	4^+, 2^+
	1279	115	1691, 1279	6^+, 4^+
	1279	706	2398, 1691	(6^+), 6^+
$^{134}_{53}$I	211	435	645, 210	unknown
$^{134}_{54}$Xe	847	406	2137, 1731	6^+, 4^+
	847	541	2272, 1731	5^+, 4^+
	847	884	1731, 847	4^+, 2^+
	847	1073	1920, 847	3^+, 2^+
$^{135}_{54}$Xe	1132	547	1678, 1132	$(7/2)^+$, $7/2^+$
	1132	837	1968, 1132	$(9/2)^+$, $7/2^+$
$^{136}_{54}$Xe	1313	197	1891, 1694	6^+, 4^+
	1313	381	1694, 1313	4^+, 2^+

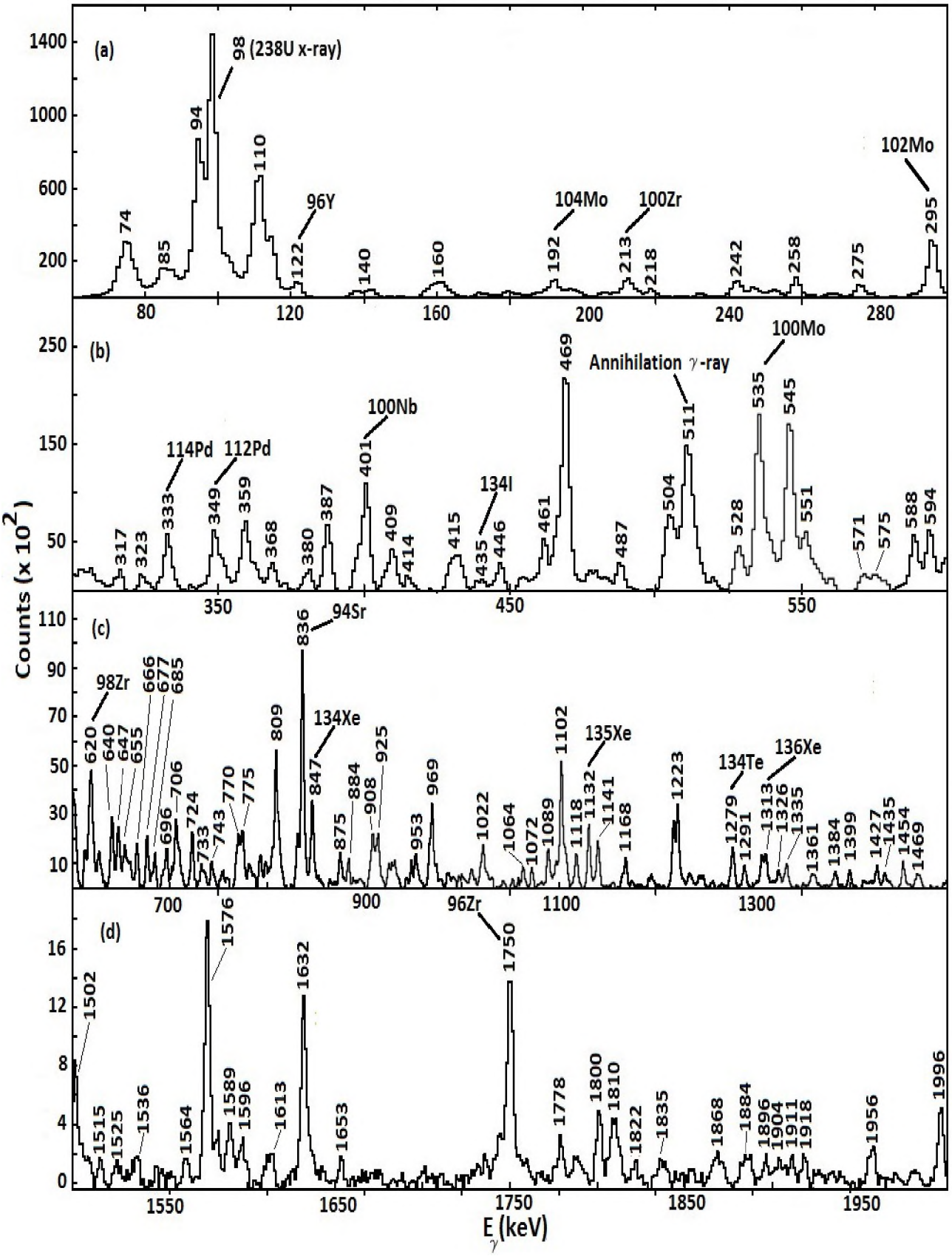

Figure 5.1: Total projection spectra in the energy ranges: 0 keV - 300 keV (Panel (a)), 300 keV - 600 keV (Panel (b)), 600keV - 1500 keV (Panel (c)) and 1500 keV - 2000 keV (Panel (d)). Peaks which were used as gates are labeled with the names of their nuclides.

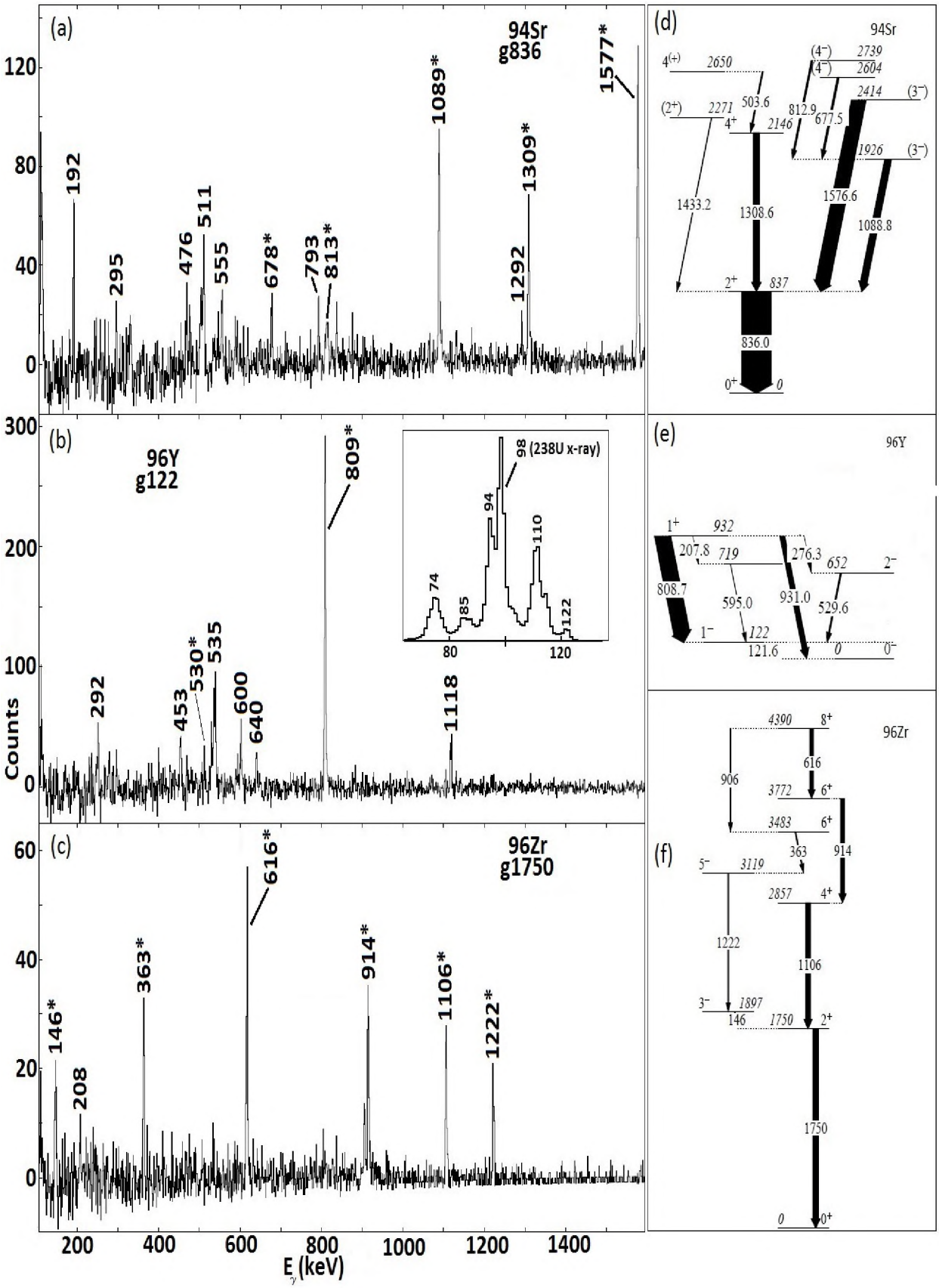

Figure 5.2: Spectra obtained by setting a gate on the the lowest transitions of $^{94}_{38}$Sr, $^{96}_{39}$Sr and $^{96}_{40}$Zr. Panel (a) shows a spectrum obtained by setting a gate on the 836 keV tansition (here labeled as g836) of $^{94}_{38}$Sr, and its level scheme is shown to the immediate right in Panel (d). Peaks with the label * represent the transitions the seen in our data for the three nuclides mentioned above. The remaining panels follow the similar interpretation. All values of energy are in keV.

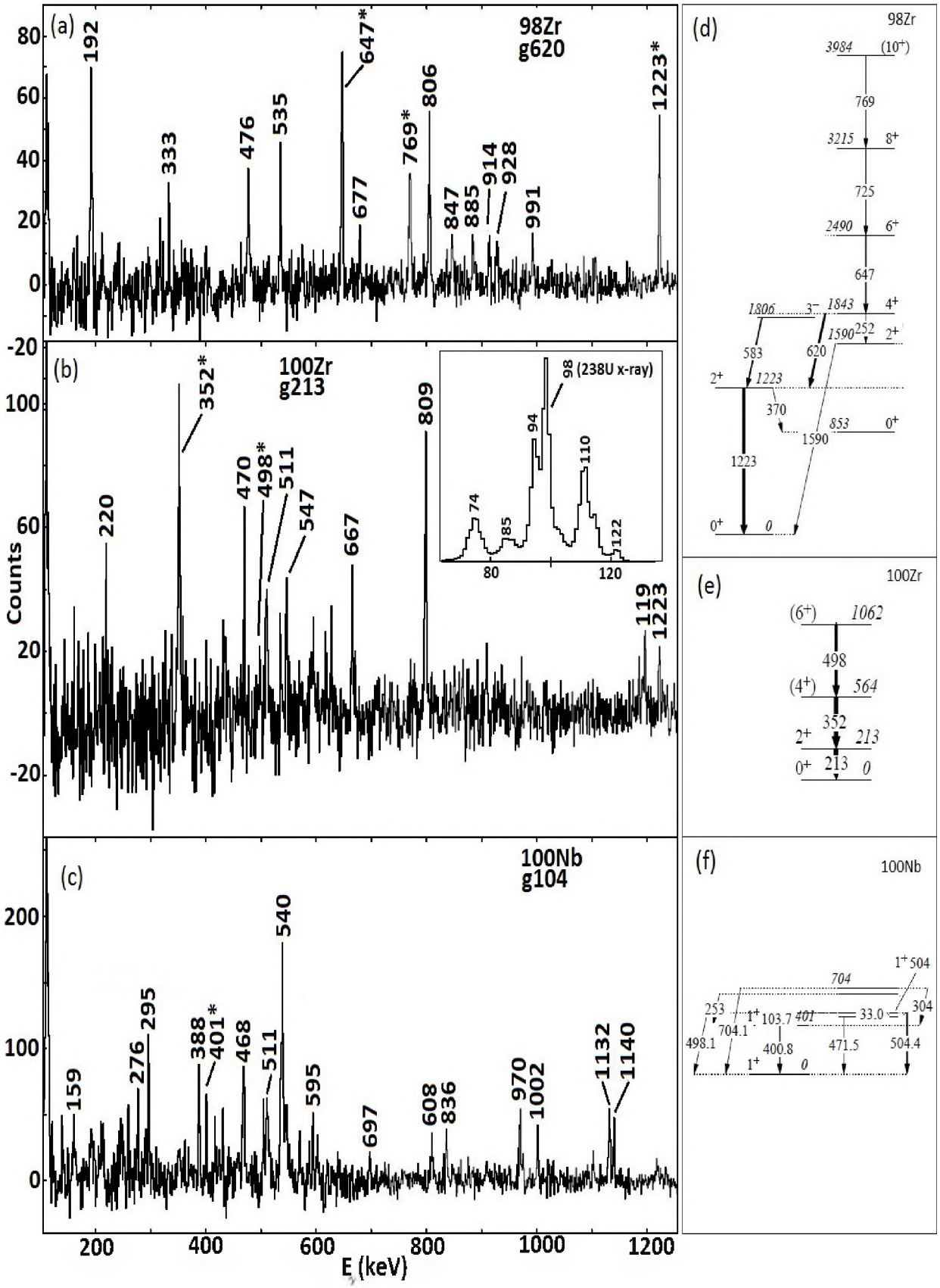

Figure 5.3: Spectra obtained by setting a gate on 620-, 213- and 104-keV transitions of $^{98}_{40}$Zr $^{100}_{40}$Zr and $^{100}_{41}$Nb respectively. Partial level schemes are shown at right. Peaks with the label * represent the transitions confirmed in the present work for the three nuclides mentioned above. The remaining panels follow the similar interpretation. All values of energy are in keV.

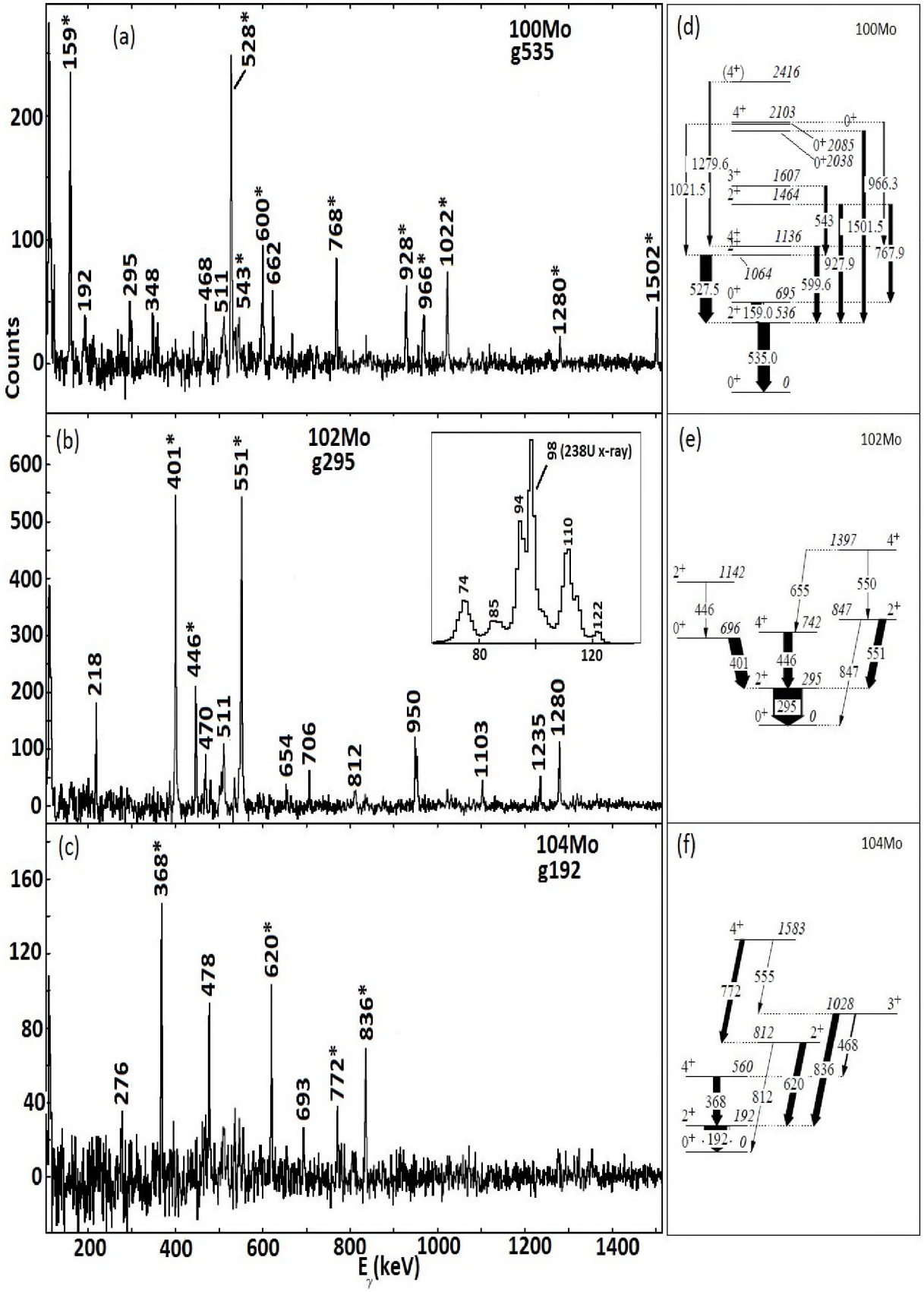

Figure 5.4: Spectra obtained by setting a gate on the the lowest transitions, and the level schemes of $^{100}_{42}$Mo, $^{102}_{42}$Mo and $^{104}_{42}$Mo. Panel (a) shows a spectrum obtained by setting a gate on the 535 keV tansition (here labelled as g535) of $^{100}_{42}$Mo, and its level scheme is shown to the immediate right in Panel (d). Peaks with the label * represent the transitions seen in our data for the three nuclides mentioned above. The remaining panels follow the similar interpretation. All values of energy are in keV.

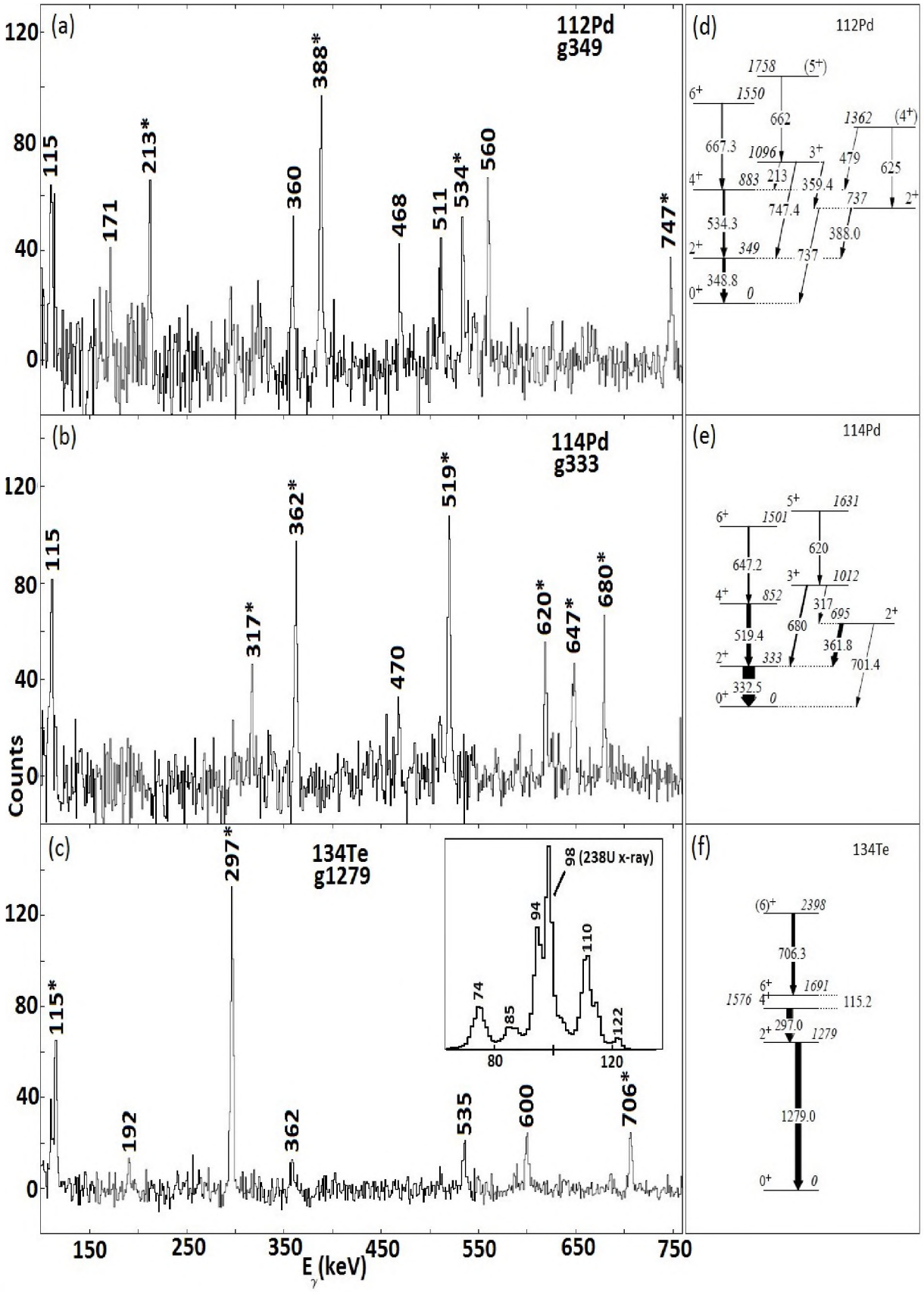

Figure 5.5: Spectra obtained by setting a gate on the the lowest transitions, and the level schemes of $^{112}_{46}$Pd, $^{114}_{46}$Pd, and $^{134}_{52}$Te. Panel (a) shows a spectrum obtained by setting a gate on the 349 keV tansition (here labelled as g349) of $^{112}_{46}$Pd, and its level scheme is shown to the immediate right in panel (d). Peaks with the label * represent the transitions seen in our data for the three nuclides mentioned above. The remaining panels follow the similar interpretation. All values of energy are in keV.

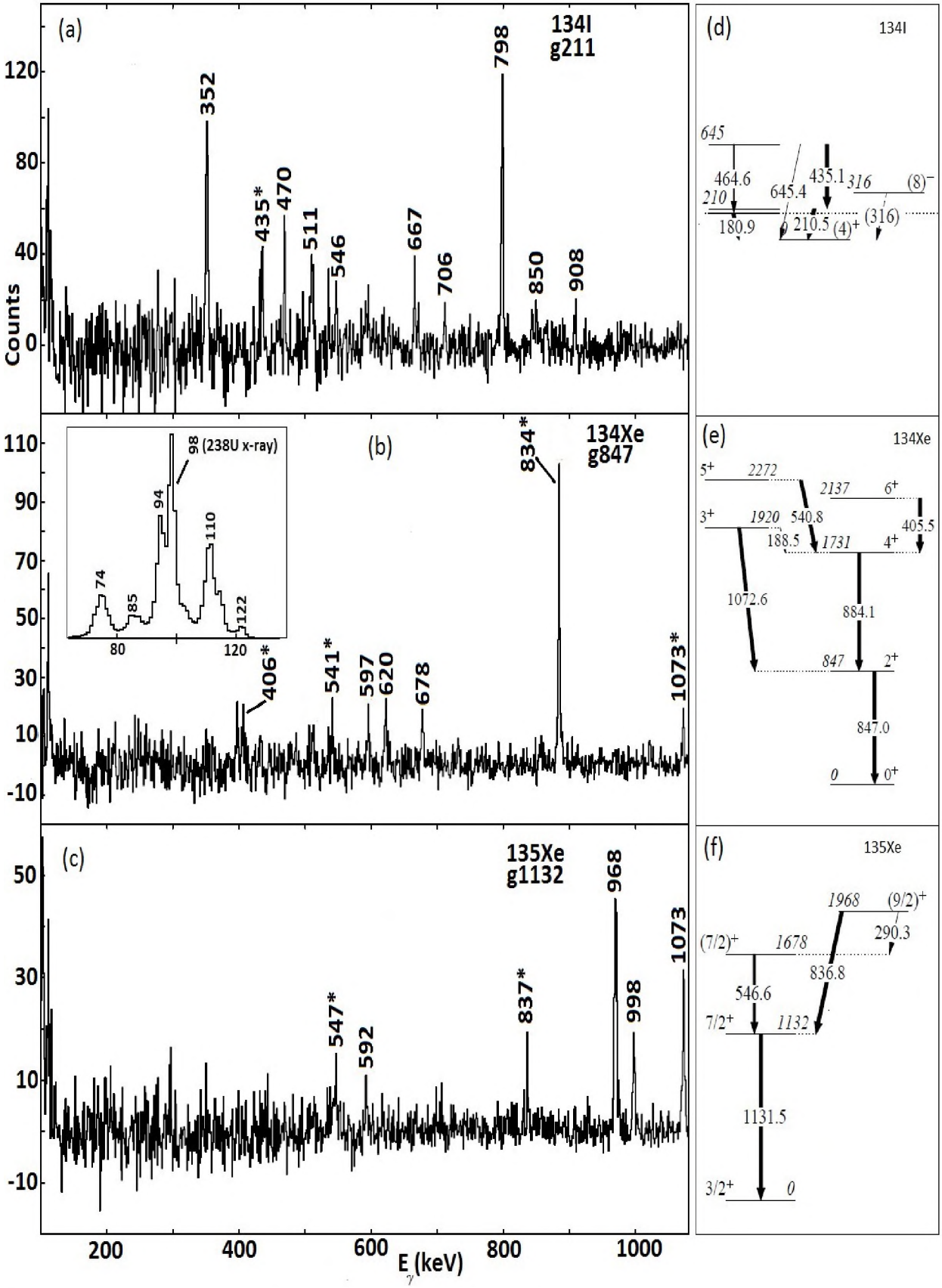

Figure 5.6: Spectra obtained by setting a gate on the the lowest transitions, and the level schemes of $^{134}_{53}$I, $^{134}_{54}$Xe and $^{135}_{53}$Xe. Panel (a) shows a spectrum obtained by setting a gate on the 211 keV tansition (here labelled as g211) of $^{134}_{53}$I, and its level scheme is shown to the immediate right in panel (d). Peaks with the label * represent the transitions seen in our data for the three nuclides mentioned above. The remaining panels follow the similar interpretation. All values of energy are in keV.

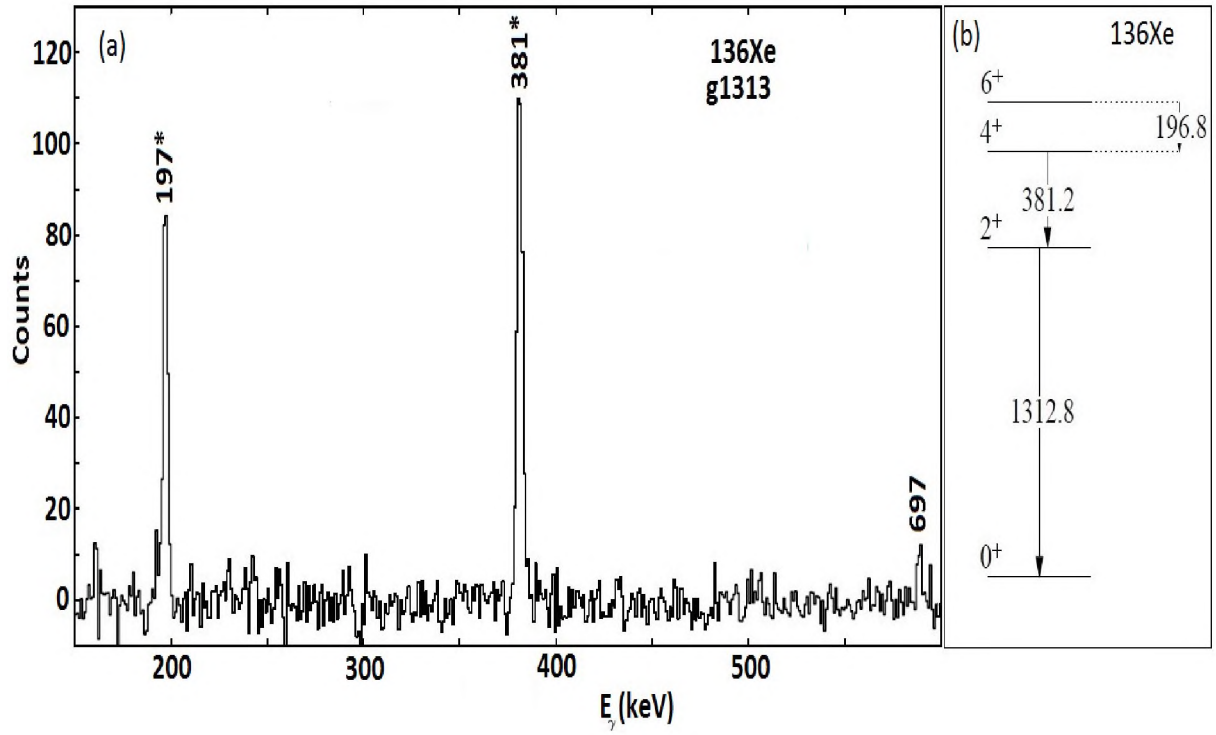

Figure 5.7: Spectrum obtained by setting a gate on the the lowest transitions, and the level schemes of $^{136}_{54}$Xe nuclides. Panel (a) shows a spectrum obtained by setting a gate on the 1313 keV tansition (here labelled as g1313) of $^{136}_{54}$Xe, and its level scheme is shown to the immediate right in panel (d). Peaks with the label * represent the transitions confirmed by the present work for $^{136}_{54}$Xe. All values of energy are in keV.

5.2 Beta decay of $^{100}_{40}$Zr

The second aim of the present work was to study beta decay of the A = 100 chain. Three nuclides with the atomic mass of 100, namely $^{100}_{40}$Zr, $^{100}_{41}$Nb and $^{100}_{42}$Mo are seen in our data, and $^{100}_{39}$Y is not seen. So, the A = 100 chain begins with $^{100}_{40}$Zr and ends with $^{100}_{42}$Mo (see Figure 5.8). In this section, therefore, a discussion of the population of $^{100}_{41}$Nb by its parent $^{100}_{40}$Zr is presented. We begin by confirming the observed transitions in $^{100}_{41}$Nb, followed by a discussion of the population of its energy levels.

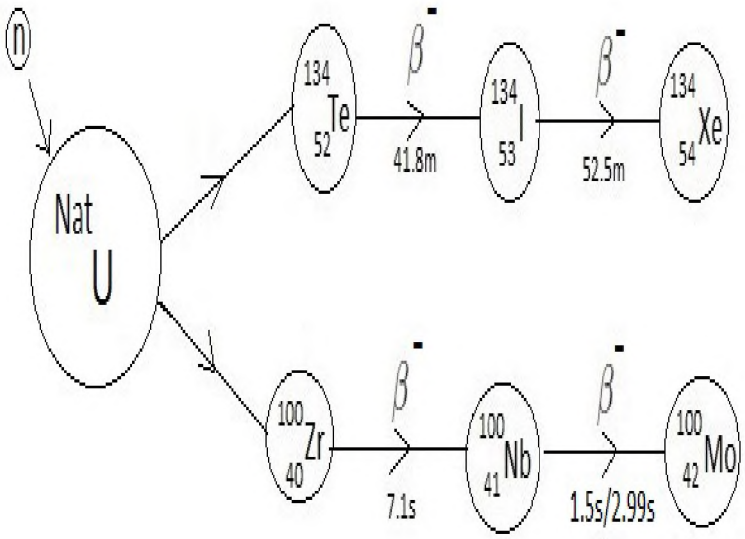

Figure 5.8: A diagrammatic representation of the decay chains generated via neutron-induced fission of natural uranium. The atomic number of consecutive nuclides increases by 1 in both the A = 100 and A =134 chains. This confirms the presence of β^- decay.

The level scheme in Figure 5.3 (f) shows that the ground-state transition in $^{100}_{41}$Nb is a 401-keV $1^+ \longrightarrow 1^+$ transition, and that the excited 1^+ state is populated by γ rays with energies 304, 253, and 104 keV. Therefore we expect these γ rays to be in coincidence with the 401-keV ground-state transition. When a gate is set on 104 keV a peak is seen at 401 keV. The 253- and 304-keV gamma transitions are not seen in the spectrum because they are not in coincidence with the gate. This confirms our suggestion that the presence of these transitions is a result of the population of the $^{100}_{41}$Nb via β^- decay of $^{100}_{40}$Zr. Also present in this decay scheme are the 704-, 504- and 498-keV transitions which are not in coincidence with any other transition. This is the reason these transitions are not observed in this work for only transitions which are in coincidence (same decay path) can be seen.

We now investigate the population of the energy levels of $^{100}_{41}$Nb via β^- decay of the 0^+ ground state in $^{100}_{40}$Zr. The spin change ΔI is given by [12]:

$$\Delta \mathrm{I} = \mid \mathrm{I}_i^{\pi} - \mathrm{I}_f^{\pi} \mid, \tag{5.1}$$

where I is the spin and π denotes the parity, subscripts i and f denote the initial and final states. In this case the I_i^π value is 0^+ of the ground state in $^{100}_{40}$Zr, and the I_f^π values are those for the confirmed energy levels of $^{100}_{41}$Nb (Figure 5.9).

Starting with the $I^\pi = 1^+$, 401-keV level of $^{100}_{41}$Nb, the spin change is $\Delta I = 1$ and there is no change in parity (i.e., $\Delta\pi = 0$). The possible values of the relative orbital angular momentum with respect to the parent state and the intrinsic spin of the electron and the antineutrino for β^- decay are $(l, s) = (0, 1), (2, 1)$. As shown in Figure 5.13 the log ft value of 4.79 is consistent with the interpretation of an allowed beta-decay. So, $(l, s) = (0, 1)$ in more likely than $(l, s) = (2, 1)$. Therefore the spin change $\Delta I = 1$ is consistent with the interpretation of an allowed Gamow Teller decay.

We now turn our attention to the 504-keV level of $^{100}_{41}$Nb. The I^π value of this level is also 1^+. Using the same argument as for the 401-keV level, the spin change $\Delta I = 1$ is also in line with the classification of an allowed Gamow Teller decay. The log ft value is 4.49 and this is indicative of an allowed beta-decay.

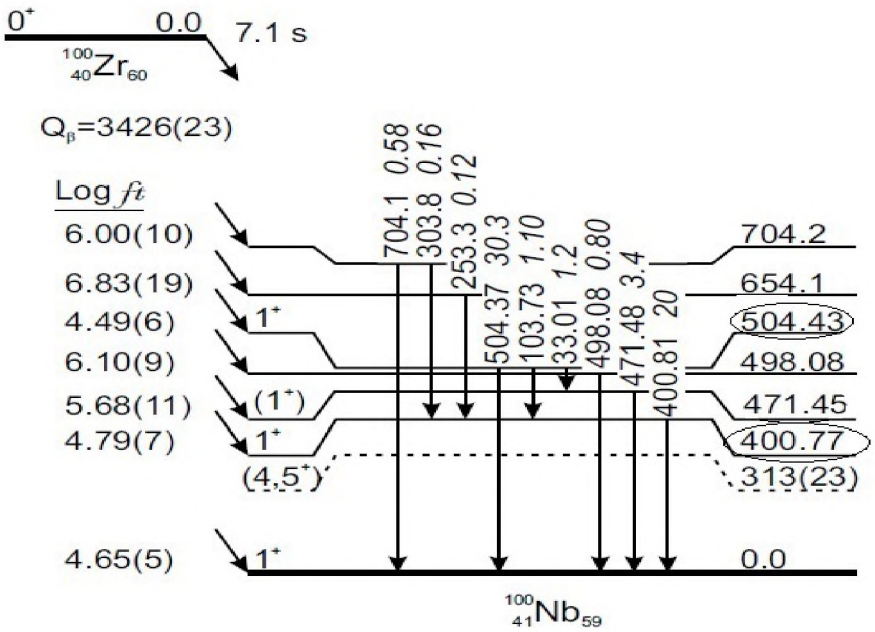

Figure 5.9: The decay scheme of $^{100}_{41}$Nb [30]. The circled energy levels have been confirmed in the present work. All values of energy are in keV. Dots represent the 313-keV isomeric state.

5.3 Beta decay of $^{100}_{41}$Nb

In this section we will discuss the population of $^{100}_{42}$Mo by $^{100}_{41}$Nb. $^{100}_{41}$Nb can populate the energy levels of its daughter $^{100}_{42}$Mo through β^- decay of the 1^+ ground state or via β^- decay of its 313-keV isomeric state, for which the tentative I^π is $(4^+, 5^+)$. Hence, two decay schemes of $^{100}_{42}$Mo are used in this discussion (Figures 5.11 and 5.12). We will also investigate the relative intensities of the 528- and 600-keV γ-lines in $^{100}_{42}$Mo. This investigation enables us to confirm if, in the present work, $^{100}_{42}$Mo is indeed populated via β^- decay of the isomeric state and ground state of $^{100}_{41}$Nb mentioned above.

5.3.1 Population of the energy levels of $^{100}_{42}$Mo

The level scheme of $^{100}_{42}$Mo confirmed in this work is shown in Figure 5.4 (d). In this level scheme the 535-keV, $2^+ \longrightarrow 0^+$ is the ground-state transition. The 159-, 528-, 600-, 928-, and 1502-keV γ rays which feed into the 536-keV energy level are strongly observed to be in coincidence with the 535-keV ground state transition, as shown in Figure 5.4 (a). A spectrum gated on 528 keV sees a strong peak at 535 keV (Figure 5.10), as expected. In this way we conclude that $^{100}_{42}$Mo is present in our data.

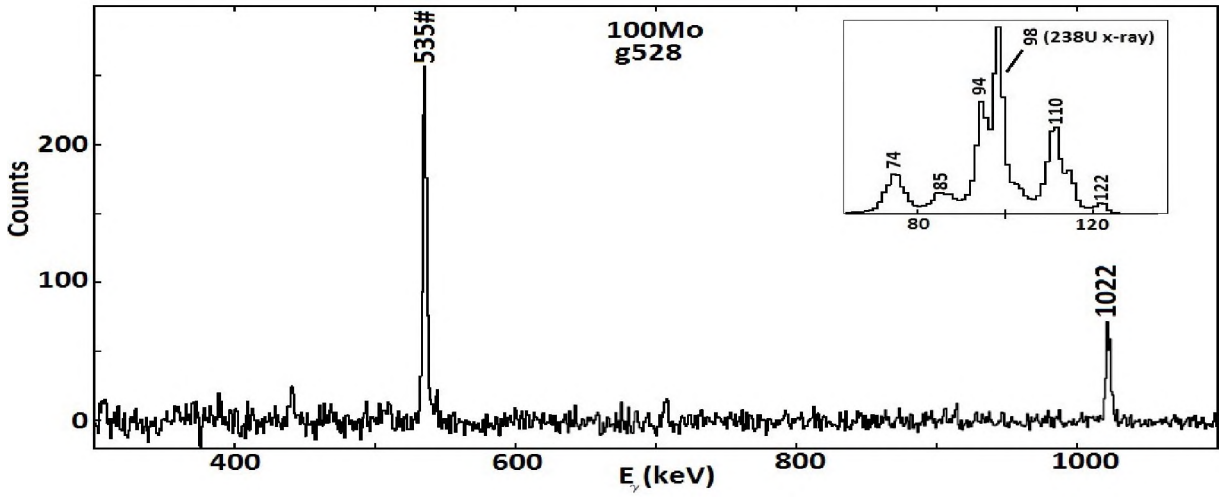

Figure 5.10: Spectrum obtained by setting a gate on the the 528-keV, $2^+ \longrightarrow 2^+$ transition of $^{100}_{42}$Mo. The 535-keV, $2^+ \longrightarrow 2^+$ transition is labelled with # symbol.

We now consider the population of $^{100}_{42}$Mo via β^- decay of the 313-keV isomeric state of $^{100}_{41}$Nb. This state has been assigned a tentative spin parity of $I_i^\pi = (4^+, 5^+)$, where parentheses indicate the values are tentative [4]. First let us consider β^- decay of the $(4^+, 5^+)$ state of $^{100}_{41}$Nb to the 2^+(536-keV) state of $^{100}_{42}$Mo. Since the initial I_i^π value is tentative, it is not known whether the parity changes or not. The spin change can be $\Delta I = 2, 3$. If the spin change is $\Delta I = 2$ then the possible values of the relative orbital angular momentum and the intrinsic spin of the electron and the antineutrino are $(l, s) = (2, 0), (1, 1)$. If the spin change is $\Delta I = 3$, the possibility is $(l, s) = (2, 1), (3, 0)$. The log ft value for this decay is 6.7 (Figure 5.14), and this can be indicative of either an allowed or first forbidden decay. Thus $(l, s) = (1, 1)$ is more likely than $(l, s) = (2, 0)$,$(2, 1), (3, 0)$. So, the change in spin $\Delta I = 2, 3$ is consistent with the interpretation of the first forbidden Gamow Teller decay. This suggests that there should be a change in parity of the parent state. Consequently, the 313-keV isomeric state of $^{100}_{41}$Nb can have I^π of $(4^-, 5^-)$.

We now focus our attention on β^- decay of the $(4^+, 5^+)$ state of $^{100}_{41}$Nb to the 0^+(695-keV) state of $^{100}_{42}$Mo. We do not know if there is a parity change. The spin change can be $\Delta I = 4, 5$. When the spin change is $\Delta I = 4$ the possible values of the relative orbital angular momentum and the intrinsic spin of the electron and the antineutrino are $(l, s) = (3, 1), (4, 0)$. And when the spin change is $\Delta I = 5$ the possibility is $(l, s) = (4, 1), (5, 0)$. The log ft value is 6.2 [12], and this seems to be consistent with the description of either an allowed decay or the first forbidden decay. So, the log ft value does not favour any of the listed (l, s) values. However $(l, s) = (3, 1)$ is more likely than $(l, s) = (4, 0), (4, 1), (5, 0)$. Therefore, the spin change $\Delta I = 4, 5$ is consistent with the interpretation of the third forbidden Gamow Teller decay. This also suggests a change in parity of the parent state.

We now consider β^- decay of the $(4^+, 5^+)$ state of $^{100}_{41}$Nb to the 2^+(1064 keV) state of

$^{100}_{42}$Mo. The spin change can be ΔI = 2, 3 and it is not known if the parity changes or not. When ΔI = 2 then the probable values of the relative orbital angular momentum and the intrinsic spin of the electron and the antineutrino are (l, s) = (2, 0), (1, 1). And when the spin change is ΔI = 3 then (l, s) = (3, 0), (2, 1). The log ft value for this state is 6.5 (Figure 5.13), and this is in line with the classification of either allowed or first forbidden decay. So, (l, s) = (1, 1) is favoured by the log ft value. Thus the change in spin ΔI = 2, 3 is consistent with an interpretation of the first forbidden Gamow Teller decay (l = 1, s = 1). This again suggests a change in parity of the parent state.

Now, let us look at β^- decay of the (4^+, 5^+) state of $^{100}_{41}$Nb to the 4^+(1136-keV) state of $^{100}_{42}$Mo. The change in spin can be ΔI = 0, 1 and we do not know if there is a parity change or not. If the spin change is ΔI = 0 then the possible values of the relative orbital angular momentum and the intrinsic spin of the electron and the antineutrino are (l, s) = (0, 0). If the spin change is ΔI = 1 then (l, s) = (0, 1), (1, 0). The log ft values is 5.9 and this is indicative of an allowed transition. This favours (l, s) = (0, 0), (0, 1). Consequently, the spin change ΔI = 0, 1 is in line with the interpretation of an allowed Fermi decay (l = 0, s = 0) and an allowed Gamow Teller decay (l = 0, s = 1) respectively. In this case, therefore, we do not expect the parity of the parent state to change.

The same argument for β^- decay of the (4^+, 5^+) state of $^{100}_{41}$Nb to the 2^+(1064 keV) state of $^{100}_{42}$Mo can be used in the population of the 2^+ (1464-keV) state via β^- decay of the (4^+, 5^+) state of $^{100}_{41}$Nb. So, the possible values of the relative orbital angular momentum and the intrinsic spin of the electron and the antineutrino are (l, s) = (2, 0), (1, 1), (3, 0), (2, 1). The log ft value of 6.2 is consistent with the classification of the first forbidden decay. This favours (l, s) = (1, 1). Therefore, the spin change ΔI = 2, 3 is in line with the interpretation of first forbidden Gamow Teller decay. So we expect a change in parity of the parent state.

We also find that the change in spin can be ΔI = 0, 1 when the (4^+, 5^+) state of $^{100}_{41}$Nb β^- decays to the 4^+ (2102-keV) state of $^{100}_{42}$Mo. Hence, the possible values of the relative orbital angular momentum and the intrinsic spin of the electron and the antineutrino are (l, s) = (0, 0), (1, 0),(0, 1). The log ft value of 5.9 is indicative of an allowed transition. Thus (l, s) = (0, 0), (0, 1) is favoured. Therefore, the spin change ΔI = 0, 1 is consistent with the interpretation of allowed Fermi decay and allowed Gamow Teller decay respectively. So, we do not expect the parity to change.

We now consider β^- decay of the (4^+, 5^+) state of $^{100}_{41}$Nb to the (4^+) 2416-keV state of $^{100}_{42}$Mo. Using the same argument as for the 4^+ (2103-keV) state, the spin change ΔI = 0, 1 is consistent with the interpretation of an allowed Fermi decay and an allowed Gamow Teller decay (l = 0, s = 1) respectively. The log ft value for this decay is 5.1. This is indicative of an allowed transition. Hence a change in parity is not expected.

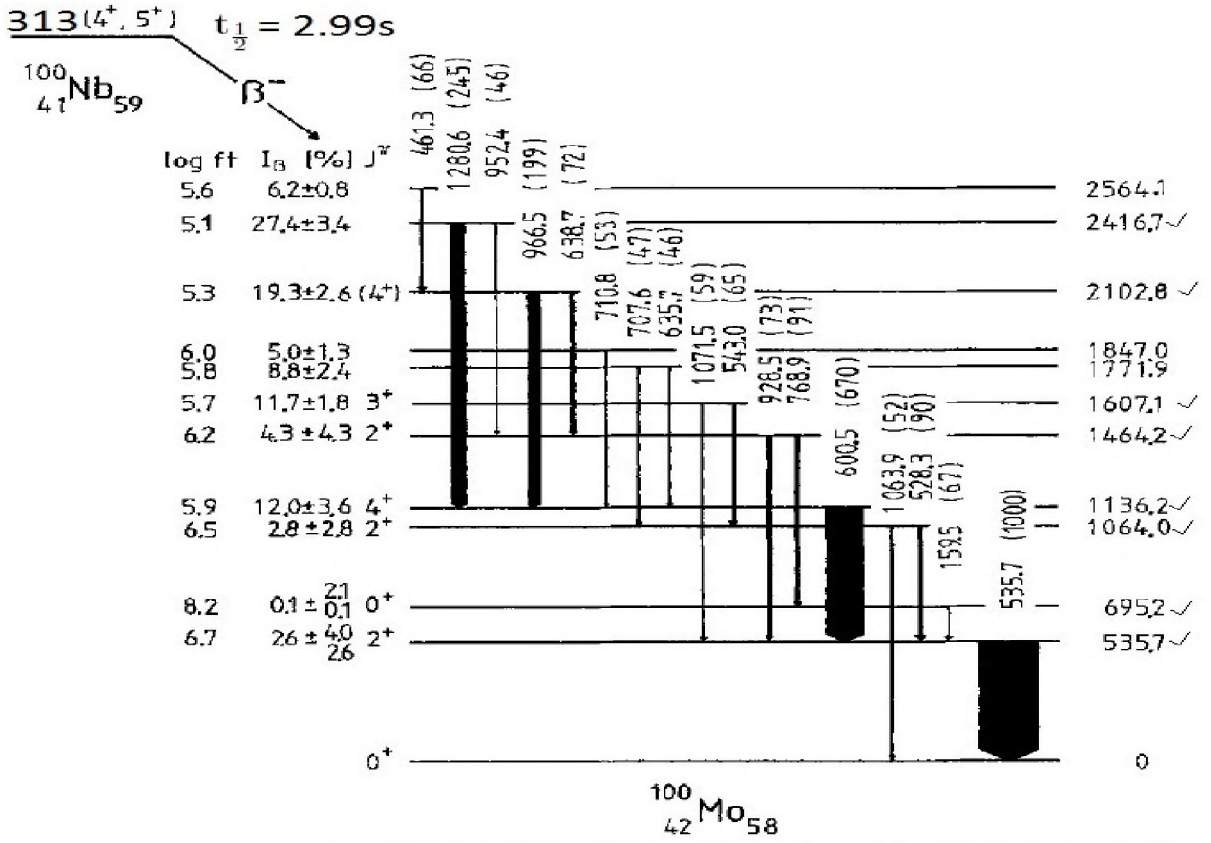

Figure 5.11: Decay scheme of $^{100}_{42}$Mo [4]. Energy levels labelled with a tick were found to be populated via the β^- decay of isomer state of $^{100}_{41}$Nb. All values of energy are in keV.

We now consider the population of $^{100}_{42}$Mo through β^- decay of the 1^+ ground state of $^{100}_{41}$Nb. In this case the initial I^π value is known to be 1^+ (Figure 5.12), and the final I^π values are those assigned to the established levels of $^{100}_{42}$Mo. We now focus our attention on β^- decay of the 1^+ ground state of $^{100}_{41}$Nb to the 2^+(536-keV) state of $^{100}_{42}$Mo. Here, the spin change is $\Delta I = 1$ and there is no change in parity (i. e., $\pi = 0$). So, the possible values of the relative orbital angular momentum and the intrinsic spin of the electron and the antineutrino are $(l, s) = (0, 1), (2, 1)$. The log ft value of 5.6 falls within the region of an allowed decay [12]. Thus $(l, s) = (0, 1)$ is favoured. Therefore the spin change $\Delta I = 1$ is in line with the interpretation of an allowed Gamow Teller decay.

We now switch our attention to β^- decay of the 1^+ ground state of $^{100}_{41}$Nb to the 0^+(695-keV) state of $^{100}_{42}$Mo. The change in spin is $\Delta I = 1$ and there is no change in parity. The

possible values of the relative orbital angular momentum and the intrinsic spin of the electron and the antineutrino are $(l, s) = (0, 1)$. The log ft value is 5.7 and this is consistent with the description of an allowed β^- decay. So, the spin change ΔI = 1 is consistent with the classification of an allowed Gamow Teller decay.

We now look at β^- decay of the 1^+ ground state of $^{100}_{41}$Nb to the 2^+(1064-keV) state of $^{100}_{42}$Mo. Applying the same argument of the population of the 2^+(536-keV) via β^- decay of the 1^+ ground state of $^{100}_{41}$Nb state to the population of 2^+(1064-keV) state, the spin change ΔI = 1 is in line with the classification of an allowed Gamow Teller decay. The log ft value is 5.85 and this is also consistent with the classification of an allowed decay.

We now consider β^- decay of the 1^+ ground state of $^{100}_{41}$Nb to the 4^+(1136-keV) state of $^{100}_{42}$Mo. The spin change is ΔI = 3 and there is no change in parity. The possible values of the relative orbital angular momentum and the intrinsic spin of the electron and the antineutrino are $(l, s) = (2, 1), (4, 1)$. The log ft value is 6.9 and this is indicative of the first forbidden transition. Thus none of the available values of the relative orbital angular momentum and the intrinsic spin of the electron is favoured by the log ft value. However, $(l, s) = (2, 1)$ is more likely than $(l, s) = (4, 1)$. So, the spin change ΔI = 3 is consistent with an interpretation of the second forbidden Gamow Teller decay.

We now turn our attention to β^- decay of the 1^+ ground state of $^{100}_{41}$Nb to the 2^+(1464-keV) state of $^{100}_{42}$Mo. There is a spin change of ΔI = 1 without a parity change. The possible values of the relative orbital angular momentum and the intrinsic spin of the electron and the antineutrino are $(l, s) = (0,1), (2, 1)$. The log ft value of 5.8 is indicative of an allowed decay. So, the spin change ΔI = 1 agrees with the interpretation of an allowed Gamow Teller decay.

We now consider β^- decay of the 1^+ ground state of $^{100}_{41}$Nb to the 0^+(2038-keV) state of

$^{100}_{42}$Mo. The spin change is ΔI = 1 and there is no change in spin. The probable values of the relative orbital angular momentum and the intrinsic spin of the electron and the antineutrino are (l, s) = (0,1). The log ft value is 5.7 and this indicates an allowed decay. Hence the spin change ΔI = 1 is consistent with the interpretation of an allowed Gamow Teller decay.

Last, we consider β^- decay of the 1^+ ground state of $^{100}_{41}$Nb to the 0^+(2085-keV) state of $^{100}_{42}$Mo. Using the same argument as for the population of the 0^+(2038-keV) state, the spin change ΔI = 1 is in line with the interpretation of an allowed Gamow Teller decay. The log ft value of 5.2 is also indicative of an allowed decay.

The 2038- and 2085-keV levels are populated via the decay of only the ground state whereas the 2103- and 2416-keV levels are populated through only the decay of an isomeric state. Therefore, it seems in this work $^{100}_{42}$Mo is populated via β^- decay of both the 1^+ ground state and the $(4^+, 5^+)$ isomeric state of $^{100}_{41}$Nb. Moreover, some decays suggest a spin change while other decays do not suggest a spin change of the isomeric state in $^{100}_{41}$Nb. So, the I^π of the isomeric state is still tentative.

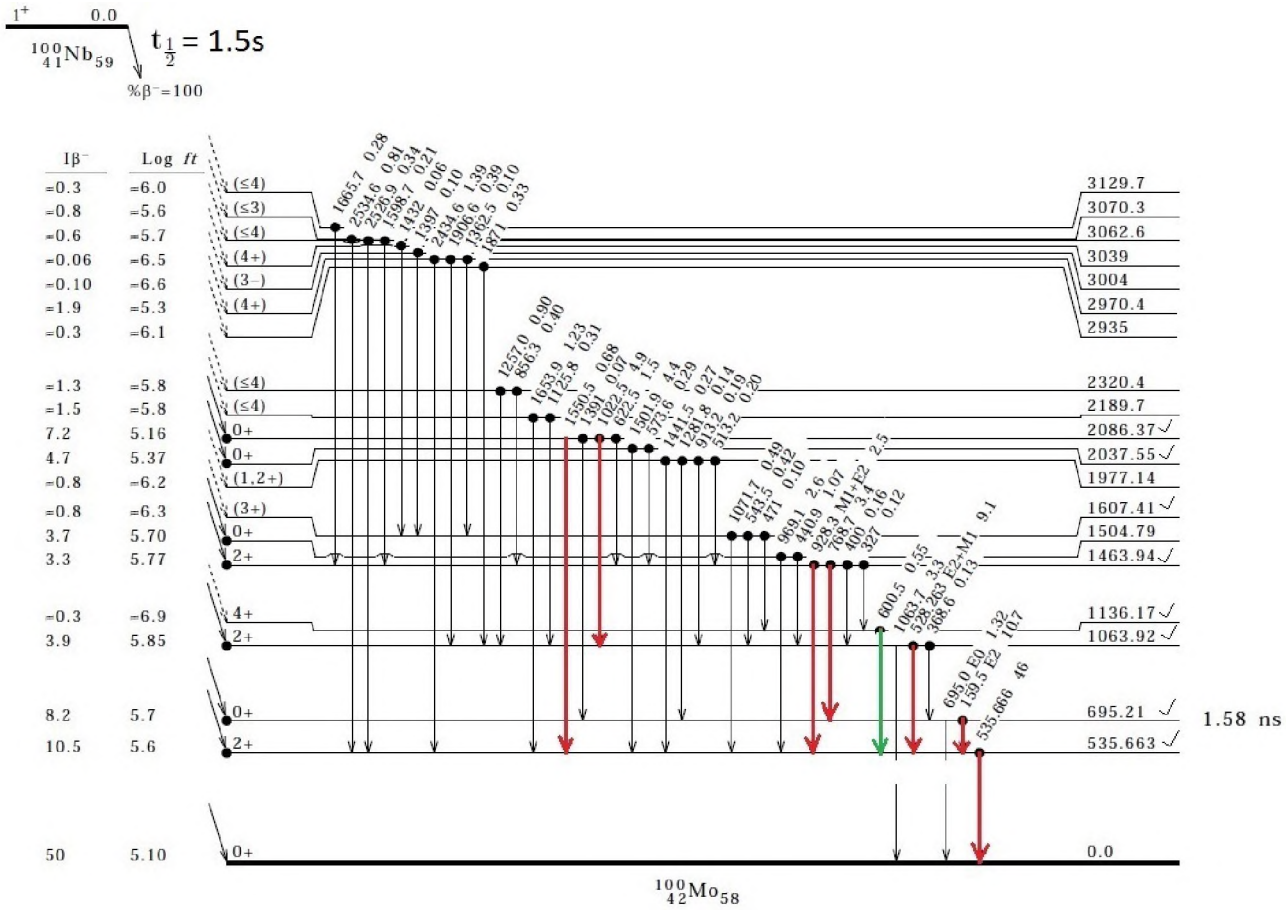

Figure 5.12: Decay scheme of $^{100}_{42}$Mo [5]. Energy levels labelled with a tick are populated via the β^- decay of the ground state of $^{100}_{42}$Nb. All values of energy are in keV.

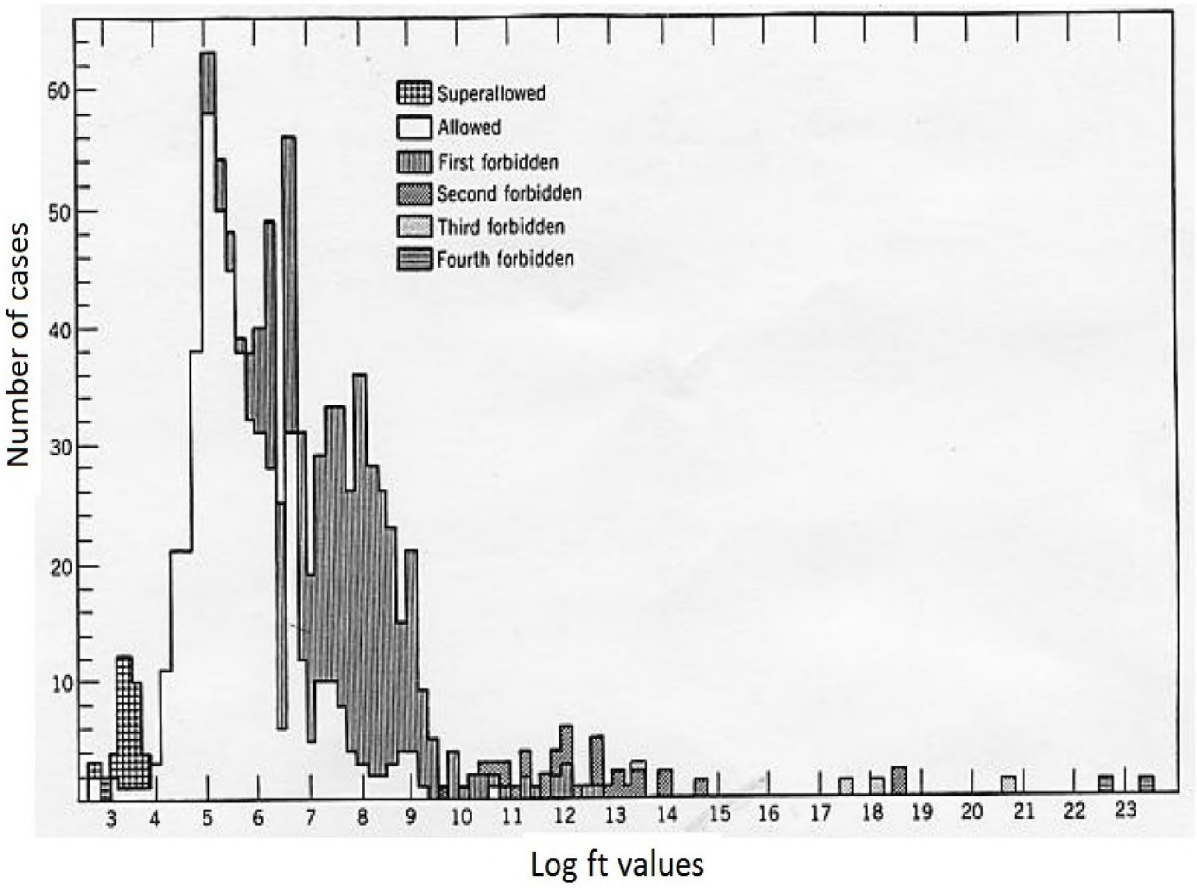

Figure 5.13: Systematics of experimental log ft values |12|.

5.3.2 The relative activities of the $(4^+, 5^+)$ isomeric state and the 1^+ ground state of $^{100}_{41}$Nb

Energy levels of $^{100}_{42}$Mo can be populated via β^- decay of the $(4^+, 5^+)$ isomeric state and the 1^+ ground state of $^{100}_{41}$Nb. So, we intend to obtain the relative activities of the isomeric state and the ground state of $^{100}_{41}$Nb when both the isomeric state and the ground state β^- decay to $^{100}_{42}$Mo.

In [4] the relative intensities I_γ of the 528- and 600-keV transitions were reported to be $I_\gamma(528) = 90(17)$ and $I_\gamma(600) = 670(17)$ normalized with respect to the strongest transition, 536 keV, which was assigned $I_\gamma(536) = 1000(23)$. That is, the ratio of the relative intensities of the 528- and 600-keV transitions is $I_\gamma(528)/I_\gamma(600) = 0.13(0.03)$. The reported intensities

include the contribution from internal conversion. However when a gate is set on the 536-keV transition, which is in coincidence with both the 528- and 600-keV transitions (Figure 5.14), we do not see the intensity ratio observed in |4|. In fact we observe the gated relative intensities to be $I_g(528) = 2047(41)$ and $I_g(600) = 928(34)$. Hence the ratio $I_g(528)/I_g(600) = 2.21(0.26)$. What could be the reason for this observed difference? The work reported in [4] involved the population of $^{100}_{42}$Mo via β^- decay of only the $(4^+, 5^+)$ isomeric state of $^{100}_{41}$Nb and not the 1^+ ground state. The observed difference, therefore, seems to indicate that in our data $^{100}_{42}$Mo is populated through β^- decay of both the isomeric state and ground state of $^{100}_{41}$Nb.

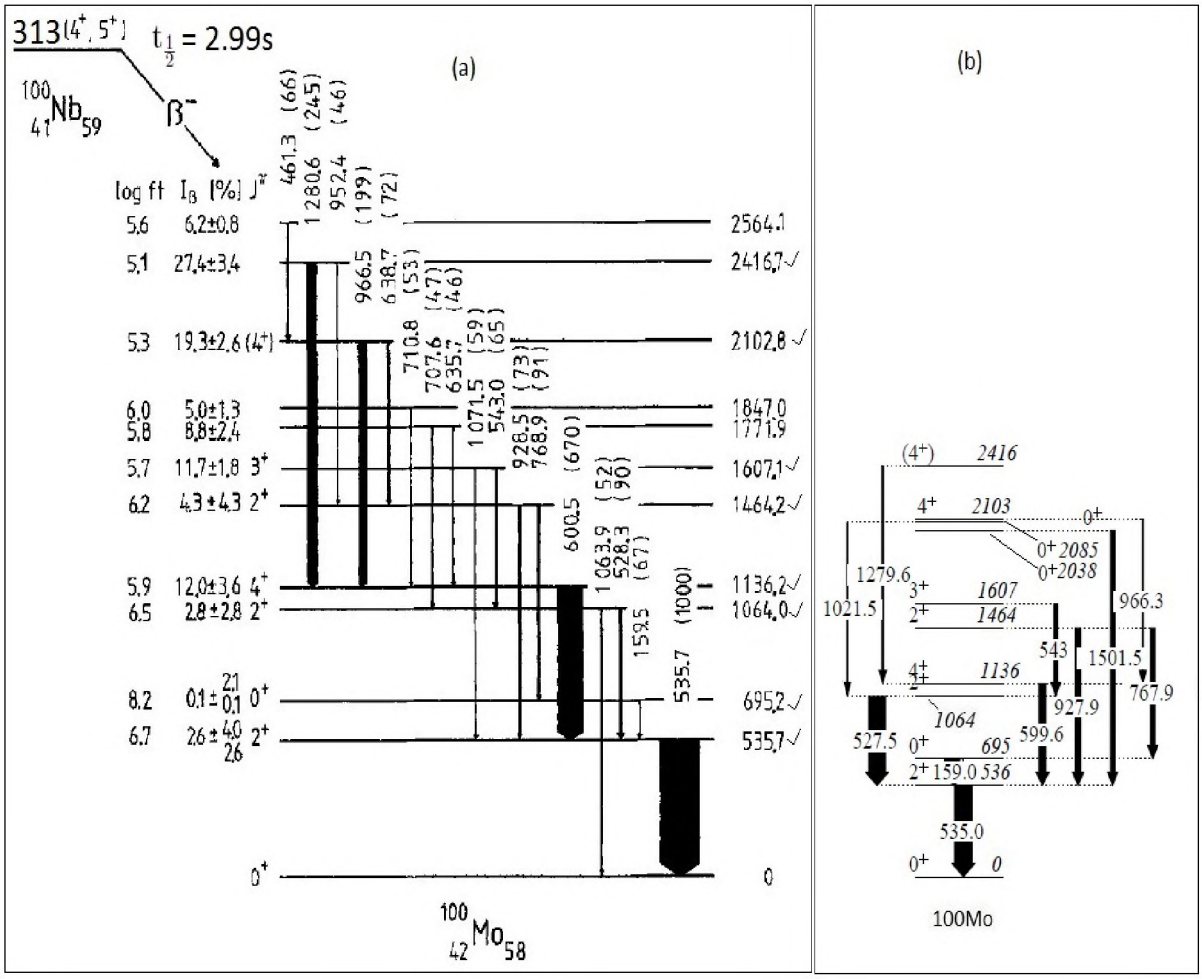

Figure 5.14: γ-ray lines of $^{100}_{42}$Mo. Panels (a) shows γ-ray lines observed in the previous work [4] while γ-ray lines seen in the present work are shown in Panel (b). The numbers in vertical parenthesis in Panel (a) are the γ-line intensities.

We now investigate the relative population of $^{100}_{42}$Mo via β^-decay of the (4^+, 5^+) isomeric state and the 1^+ ground state of $^{100}_{41}$Nb (Figures 5.14, 5.15). It is known that 2.8% of the isomeric state [4] and 3.9% of the ground state [5] of $^{100}_{41}$Nb β^- decay to the 1064-keV level of $^{100}_{42}$Mo. This leads to the following equation:

$$\mathrm{I}_\beta(1064) = \left(\frac{2.8}{100}\right)\mathrm{B} + \left(\frac{3.9}{100}\right)\mathrm{C}. \tag{5.2}$$

Here B and C denote the respective relative β^- decay rates of the (4^+, 5^+) isomeric state and the 1^+ ground state of $^{100}_{41}$Nb, which β^- decay to $^{100}_{42}$Mo. The coefficients of B and C denote the known relative intensities with which the 1064-keV state is fed via β^- decay from the isomeric state and the ground state of $^{100}_{41}$Nb respectively. $\mathrm{I}_\beta(1064)$ is the relative feeding intensity for the population of the 4^+, 1064-keV state when $^{100}_{41}$Nb β^- decays to $^{100}_{42}$Mo and is equal to the difference between the relative intensities of the γ-rays de-exciting and feeding the 1064-keV state, gated at 536 keV. Thus:

$$\mathrm{I}_\beta(1064) = \mathrm{I}_{\mathrm{out}} - \mathrm{I}_{\mathrm{in}} \tag{5.3}$$

where $\mathrm{I}_{\mathrm{out}}$ and I_{in} are the respective intensities of the γ rays de-exciting and feeding the 1064-keV state.

The 4^+, 1136-keV state in $^{100}_{42}$Mo is fed through 12% and 0.3% β^- decay of the isomeric state and ground state of $^{100}_{41}$Nb (Figure 5.12, 5.14). Thus:

$$\mathrm{I}_\beta(1136) = \left(\frac{12}{100}\right)\mathrm{B} + \left(\frac{0.3}{100}\right)\mathrm{C}, \tag{5.4}$$

where the coefficients of B and C denote the respective known relative intensities with which

the 1136-keV state in $^{100}_{42}$Mo is fed via β^- decay of the isomeric state and the ground state of $^{100}_{41}$Nb. $I_\beta(1136)$ is the relative feeding intensity for the population of the 4^+, 1136-keV state when $^{100}_{41}$Nb β^- decays to $^{100}_{42}$Mo and is equal to the difference between the relative intensities of the γ-rays de-exciting and feeding the 1136-keV state, gated at 536 keV.

From the 1064- and 1136-keV states we have:

$$\begin{aligned} I_\beta(1064) &= I_g(528) - I_g(544) - I_g(708) - I_g(1022) && (5.5)\\ &= 2047(41) - 246(28) - 932(32) && (5.6)\\ &= 869(59) && (5.7) \end{aligned}$$

and

$$\begin{aligned} I_\beta(1136) &= I_g(600) - I_g(966) - I_g(1280) && (5.8)\\ &= 928(34) - 260(34) - 270(20) && (5.9)\\ &= 398(52). && (5.10) \end{aligned}$$

The values of the gated intensities are listed in Table 5.4. The peak at 708 keV is very weak. So the relative intensity $I_g(708)$ is negligible.

Table 5.4: Relative intensities of γ rays in $^{100}_{42}$Mo when a gate is set on 536 keV. The error was obtained from the Radware fitting procedures for gamma-ray intensity.

E_γ (keV)	Relative intensity	Error
528	2047	41
544	246	28
600	928	34
966	260	34
1022	932	32
1280	270	20

Consequently, Equations 5.2 and 5.4 become:

$$869(59) = \left(\frac{2.8}{100}\right) \mathrm{B} + \left(\frac{3.9}{100}\right) \mathrm{C}, \tag{5.11}$$

and

$$398(52) = \left(\frac{12}{100}\right) \mathrm{B} + \left(\frac{0.3}{100}\right) \mathrm{C} \tag{5.12}$$

respectively.

The activities are found to be B = 2810(403) and C = 20265(1224). These values suggest that in our data $^{100}_{42}$Mo is populated via β^- decay of both the isomeric state and ground state of $^{100}_{41}$Nb. Moreover, this result can mean that in the A = 100 ($^{100}_{40}$Zr - $^{100}_{41}$Nb - $^{100}_{42}$Mo) chain the ground state of $^{100}_{41}$Nb is more populated than its isomeric state through β^- decay of $^{100}_{40}$Zr. In turn the ground state of $^{100}_{41}$Nb populates the energy levels of $^{100}_{42}$Mo more strongly hence B $<$ C. Indeed, [3] mentions that for an odd-odd nucleus which has a ground state and an isomeric state with a spin difference greater that 3 (in this case $^{100}_{41}$Nb, see Figure 5.9), the even-even parent (in this work $^{100}_{40}$Zr) will populate the energy level with the lowest spin (here, the ground state of $^{100}_{41}$Nb) with higher probability than the isomeric state.

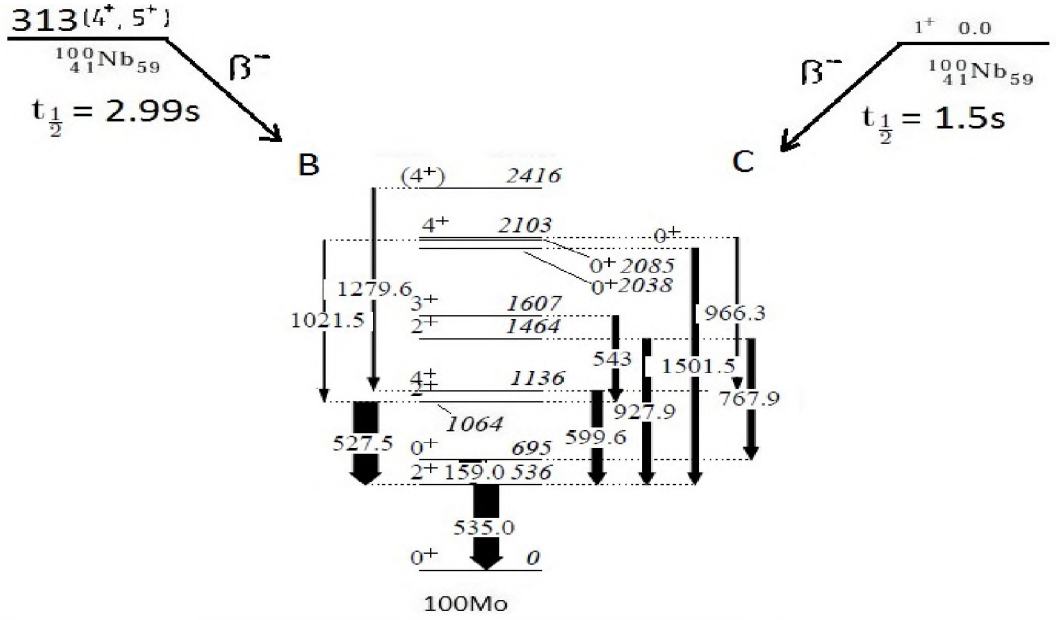

Figure 5.15: The relative rates of β^- decay of $^{100}_{41}$Nb to $^{100}_{42}$Mo. B is the rate of β^- decay of $^{100}_{41}$Nb$(4^+, 5^+)$ to $^{100}_{42}$Mo while C is the relative rate of β^- decay of $^{100}_{41}$Nb$(1^+)$to $^{100}_{42}$Mo.

5.4 Relative intensities of the γ-ray lines in $^{100}_{42}$Mo

In this work we also aimed to investigate how the relative intensities of the γ-ray lines vary as a function of time in $^{100}_{42}$Mo. This investigation enables us to model the intensity profiles of these γ-ray lines with the variation of the activity as a function of time of the $(4^+, 5^+)$ isomeric state and 1^+ ground state in $^{100}_{41}$Nb which is a parent of $^{100}_{42}$Mo. Since the excited states only live in orders of picoseconds, this investigation is also instrumental in the study of the population of energy states of $^{100}_{42}$Mo via β^- decay of the isomeric state and ground state of $^{100}_{41}$Nb. In this section we present and discuss the findings for the six γ-ray lines of 159, 528, 600, 768 928 and 1502 keV, which are in coincidence with the 536-keV gate.

The plots of the relative intensities against time are shown in Figures 5.18 , 5.19 and 5.20. It can be seen in Figure 5.18 that the relative intensity of the 159-keV γ-ray line increases from 2s and reaches the maximum value in 4s, thereafter it decreases rapidly. A similar trend is observed in the variation of the relative intensities against time of the 528-,

768-, 928- and 1502-keV γ-ray lines. However, the relative intensity of the 600-keV γ-ray line decreases steadily between 2s and 24s.

The population of $^{100}_{42}$Mo depends on the activity of $^{100}_{41}$Nb. So, we expect the relative intensities of the six γ-ray lines mentioned above to be proportional to the activity of $^{100}_{41}$Nb. Therefore the variation of this activity as a function of time can be compared to the variation of the relative intensity of the γ-ray lines against time.

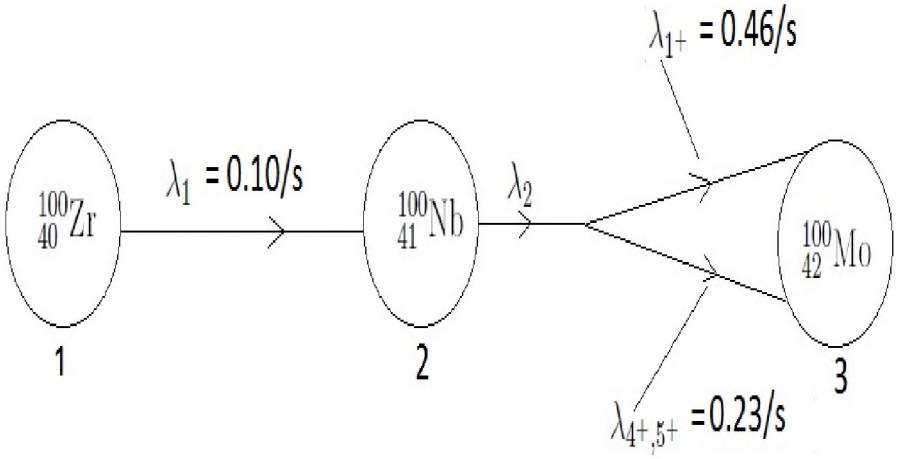

Figure 5.16: A diagrammatic representation of decay constants of $^{100}_{40}$Zr, $^{100}_{41}$Nb and $^{100}_{42}$Mo in the A = 100 chain.

Using the Bateman equations |12| (Equations C.1 and C.3 in Appendix C) the activity, $\mathscr{A}_2$, of $^{100}_{41}$Nb in the A = 100 decay chain (Figure 5.16) is given as

$$\mathscr{A}_2 = N_0 \left(c_1 e^{-\lambda_1 t} + c_2 e^{-\lambda_2 t} \right) \tag{5.13}$$

where

$$c_1 = \frac{\lambda_1 \lambda_2}{(\lambda_2 - \lambda_1)}, \tag{5.14}$$

and

$$c_2 = \frac{\lambda_1 \lambda_2}{(\lambda_1 - \lambda_2)}. \tag{5.15}$$

Here λ_1 and λ_2 are the respective decay constants of $^{100}_{40}$Zr and $^{100}_{41}$Nb whose values are listed in Table 5.5.

Table 5.5: Mean lives and decay constants of $^{100}_{41}$Nb and $^{100}_{42}$Mo. λ_2 has three values which denote the decay constants of the 1^+ ground state (λ_{1^+}), the (4^+, 5^+) isomeric state ($\lambda_{4^+,5^+}$) and the average decay constant (λ_{avg}) in $^{100}_{41}$Nb (Figure 5.17).

τ_1 (s)	τ_2 (s)	λ_1	λ_2
10.24	2.16	0.10	0.46
	4.31		0.23
	3.24		0.31

Using Equation 5.13 we obtained plots which describe the variation of the activity of the ground state and isomeric state in $^{100}_{41}$Nb as a function of time, as shown in Figure 5.17. One can see that the activities of the 1^+ ground state increases from $t = 1$ and reaches the maximum value at t = 4s, thereafter it decreases rapidly. The activity of the isomeric state increases from 1s and reaches the maximum value in 6s and then decreases rapidly. It seems the relative intensities of γ-ray lines in $^{100}_{42}$Mo track the predicted activities of the isomeric state and the ground state of $^{100}_{41}$Nb in three ways:

1. The intensity profiles of the 159- and 928-keV γ-ray lines increase up to a maximum value in 4s, and thereafter the intensities fall rapidly. This is consistent with the variation against time of the predicted activity of the 1^+ ground state in $^{100}_{41}$Nb. So, this is an indication that the 0^+, 696-keV state, and the 2^+, 1064-keV state in $^{100}_{42}$Mo (listed in Table 5.6) are populated via β^- decay of the ground state of $^{100}_{41}$Nb.

2. On the other hand the intensity profiles of the 528-, 768- and 1502-keV γ-ray lines increase up to the maximum value in 6s, thereafter the intensities decrease rapidly. This is in line

with the variation as a function of time of the predicted activity of the $(4^+, 5^+)$ isomeric state in $^{100}_{41}$Nb. Hence, this is evidence that the states of 1064, 1464 and 2086 keV in $^{100}_{42}$Mo are fed through β^- decay of the isomeric state of $^{100}_{41}$Nb.

3. The intensity profile of the 600-keV γ-ray line is consistent with variation of the activities of both the isomeric state and ground state. So, this suggests that the 1136-keV state is populated via β^- decay of both the isomeric and the ground state of $^{100}_{41}$Nb.

All in all these results confirm that in our data $^{100}_{42}$Mo is populated via β^- decay of both the 1^+ ground state and the $(4^+, 5^+)$ isomeric state of $^{100}_{41}$Nb.

Table 5.6: The known intensities for the energy states of $^{100}_{42}$Mo when the $(4^+, 5^+)$ isomeric state and the 1^+ ground state(GS) in $^{100}_{41}$Nb β^- decay to $^{100}_{42}$Mo.

E_γ(keV)	State(keV)	I_β(isomer) [4]	I_β(GS) [5]
159	695	0.1(2.1)	8.2
528	1064	2.8(2.8)	3.9
600	1136	12.0(3.6)	0.3
768	1464	4.3(4.3)	3.3
928	1464	4.3(4.3)	3.3
1502	2086	unknown	7.2

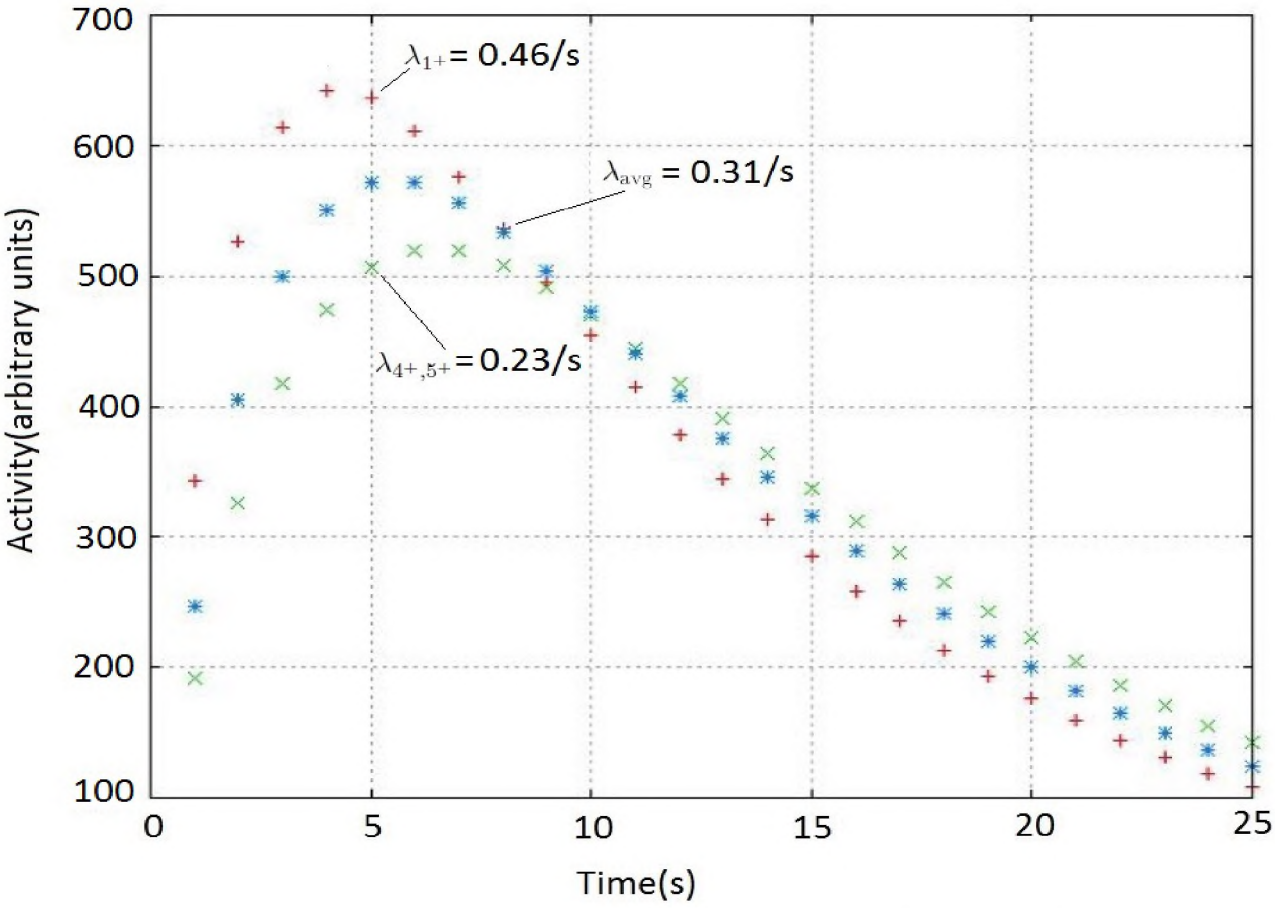

Figure 5.17: Variation of the activity of $^{100}_{41}$Nb as a function of time.

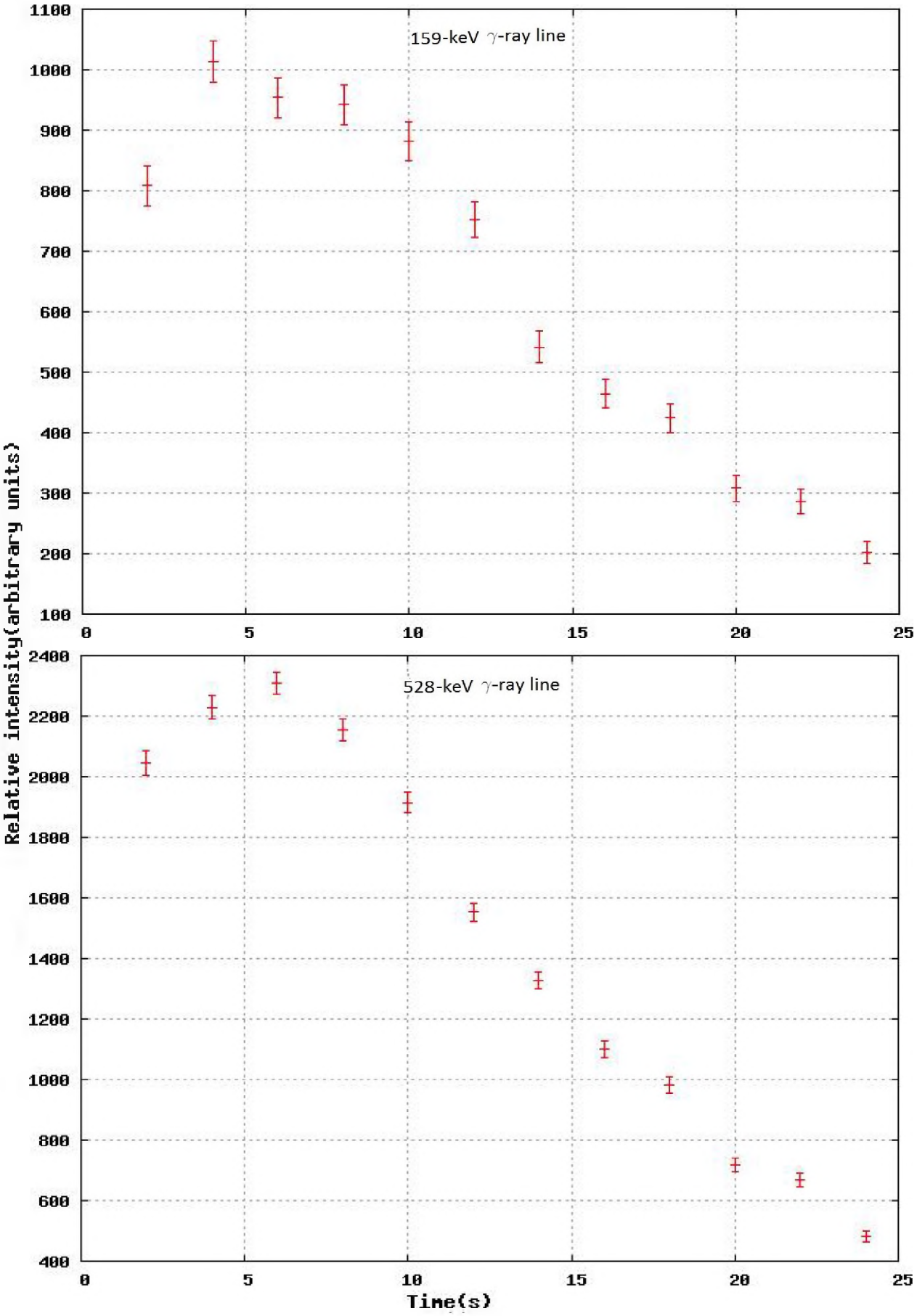

Figure 5.18: Variation of the relative intensity as a function of time.

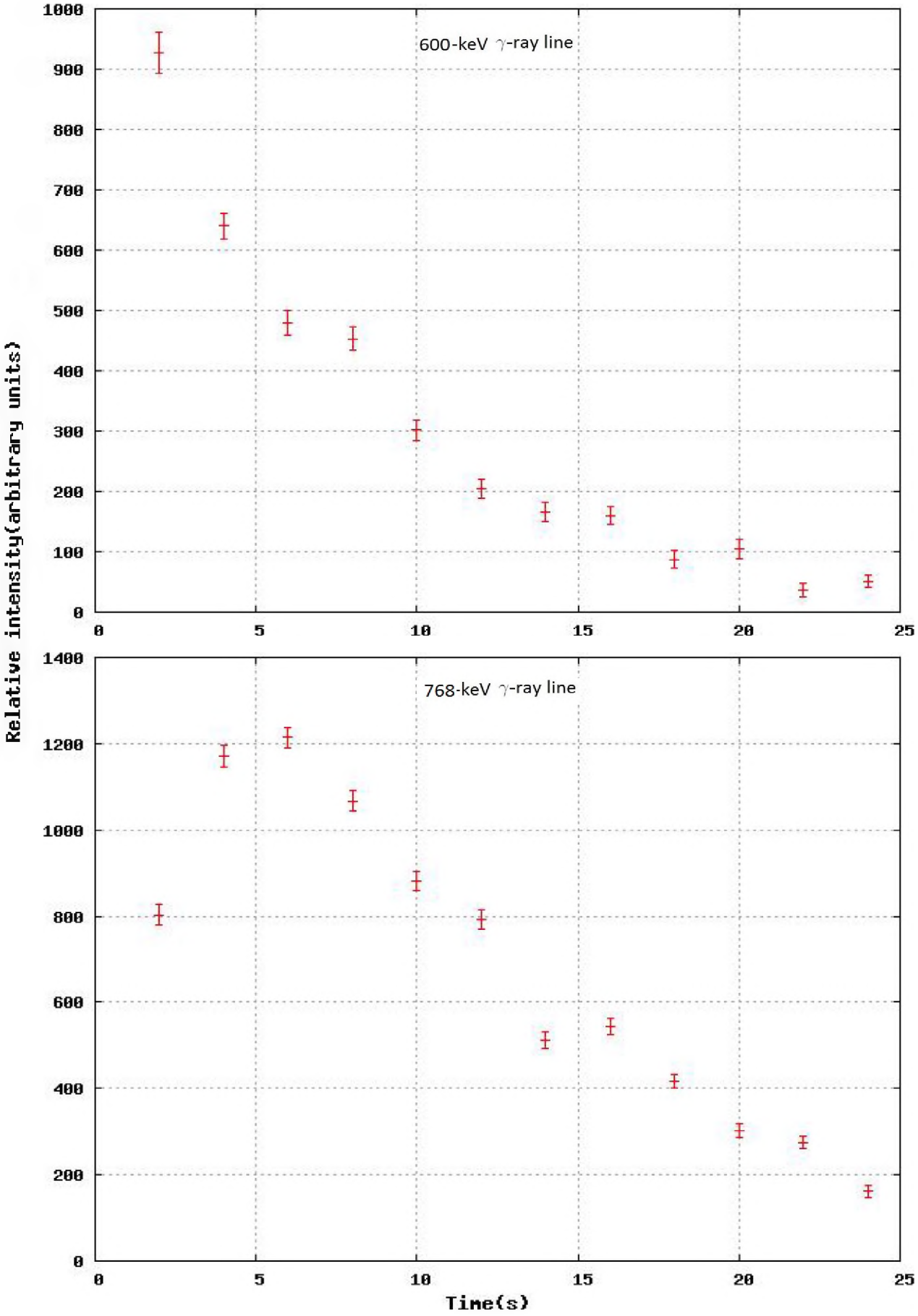

Figure 5.19: Variation of the relative intensity as a function of time.

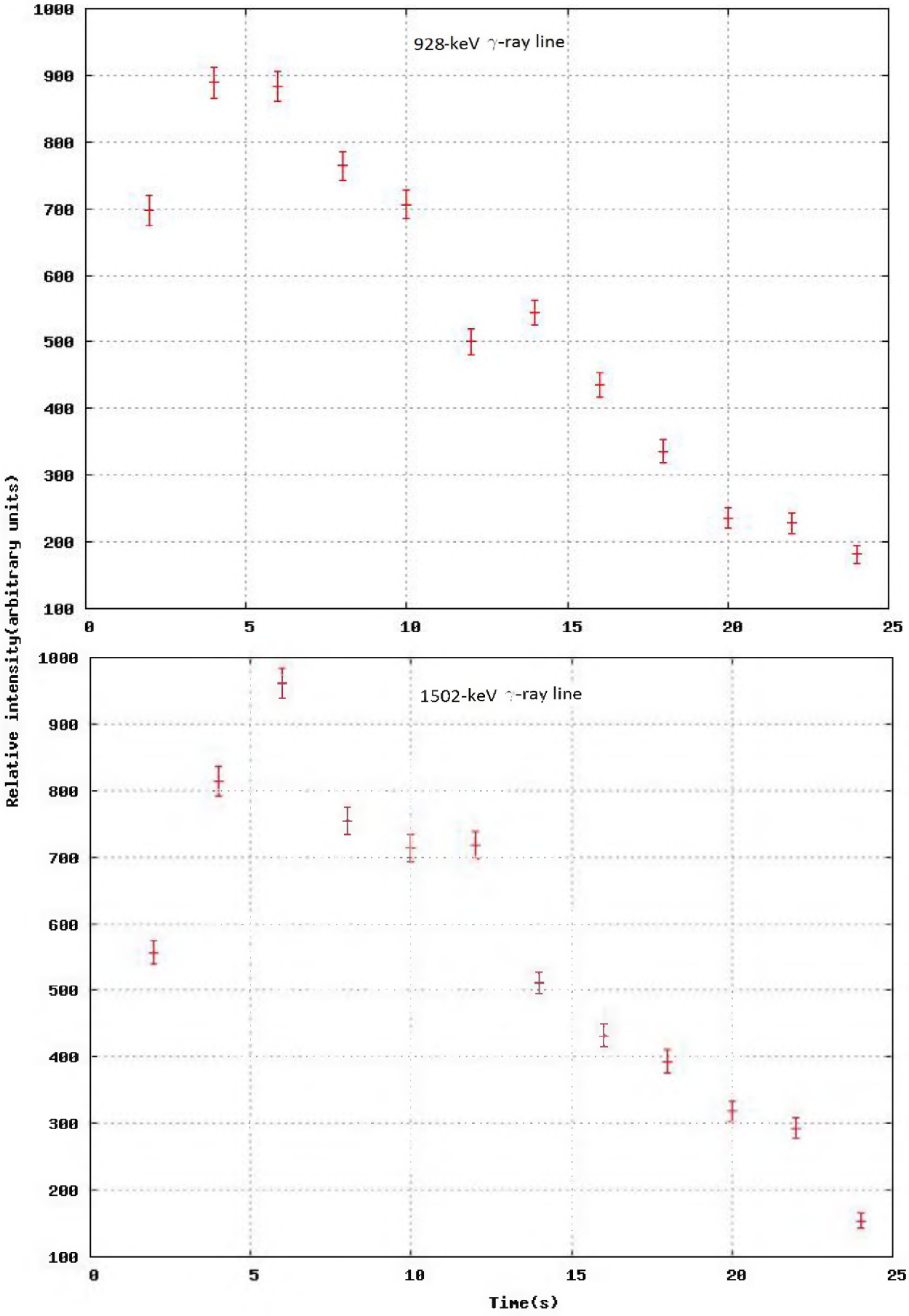

Figure 5.20: Variation of the relative intensity as a function of time.

5.5 Configuration assignment in $^{100}_{42}$Mo and $^{100}_{40}$Zr

First we look at the configuration assignment in $^{100}_{42}$Mo. The overall experimental quadrupole-deformation parameter, $\beta_2 = 0.231$ of $^{100}_{42}$Mo [39] was used to determine the positions of the Fermi surfaces for the neutron and proton. The Nilsson orbital nearest the neutron Fermi surface is likely $[550]\frac{1}{2}^-$ of the $h_{\frac{11}{2}}$ parentage while the Nilsson orbital nearest the proton Fermi surface is likely $[422]\frac{5}{2}^+$ of the $g_{\frac{9}{2}}$ parentage (refer to Figures 5.21, 5.22).

We now consider the configuration assignment in $^{100}_{40}$Zr. Using the deformation parameter $\beta_2 = 0.355$ [40] of $^{100}_{40}$Zr, the Nilsson orbital nearest the neutron Fermi surface is likely $[541]\frac{3}{2}^-$ of the $h_{\frac{11}{2}}$ parentage whereas the Nilsson orbital nearest the proton Fermi surface seem to be $[301]\frac{3}{2}^-$ of the $g_{\frac{9}{2}}$ parentage.

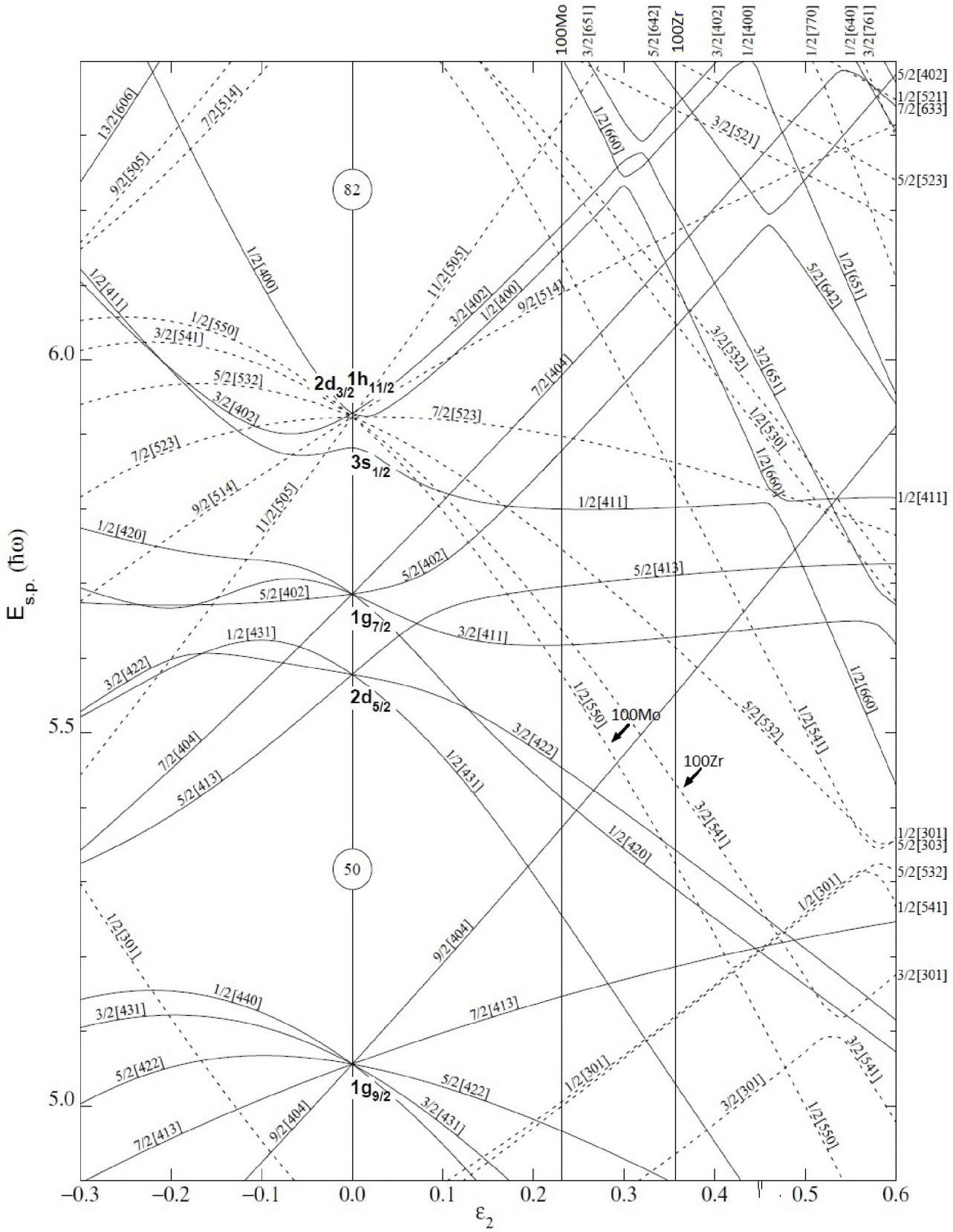

Figure 5.21: Nilsson diagram for neutrons, $50 \leq N \leq 82$ ($\varepsilon_4 = \varepsilon_2^2/6$) [17]. The arrows indicate the Fermi surface positions for $^{100}_{42}$Mo and $^{100}_{42}$Zr.

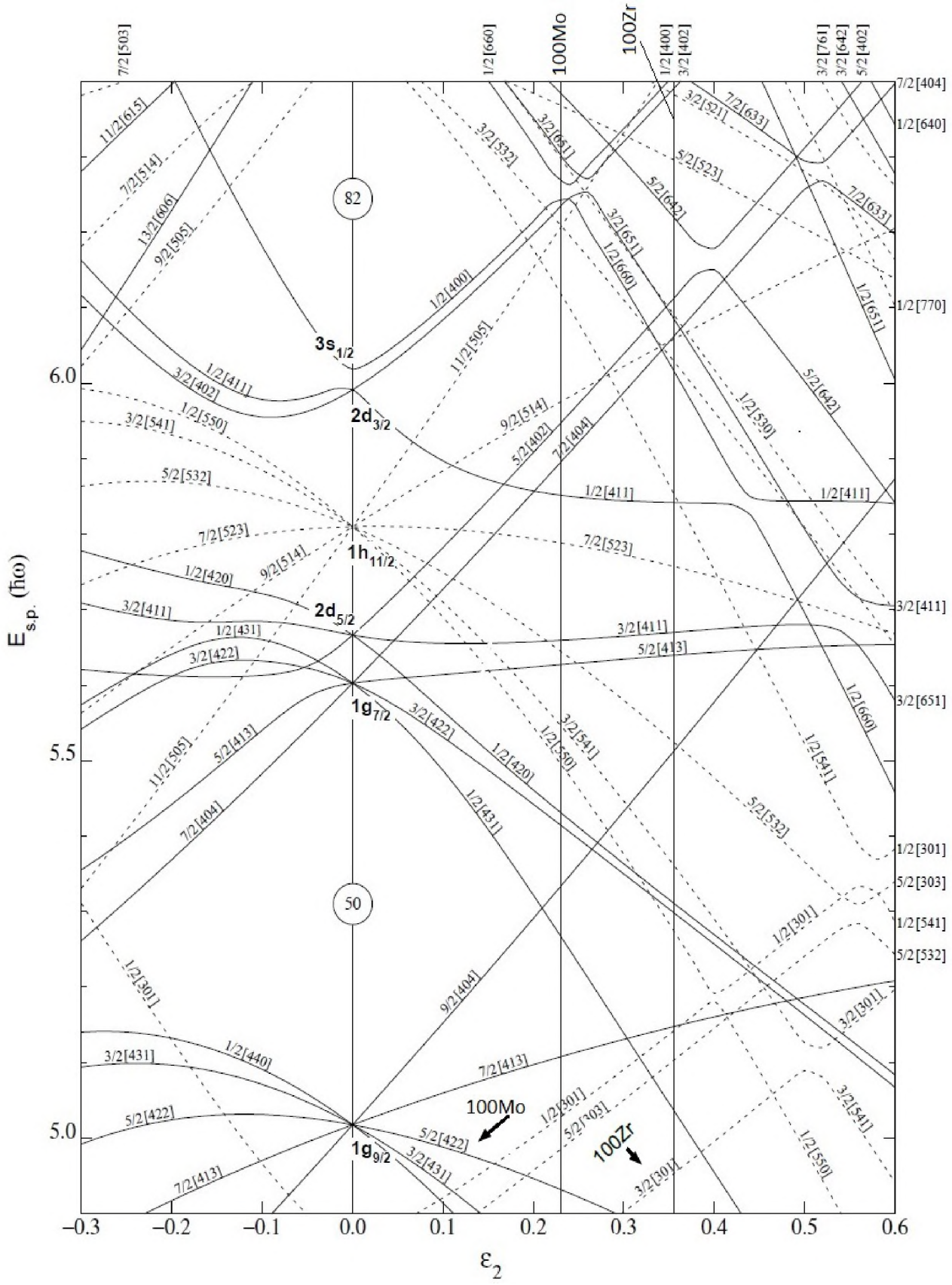

Figure 5.22: Nilsson diagram for protons, $50 \leq Z \leq 82$ ($\varepsilon_4 = \varepsilon_2^2/6$) [17]. The arrows indicate the Fermi surface positions for $^{100}_{42}$Mo and $^{100}_{42}$Zr.

Chapter 6

Conclusion and future work

γ-γ coincidence analysis has been used to identify fission products which were produced through the neutron-induced fission of natural uranium. Sixteen fission products ranging from A = 94 to A = 136 have been found. Among these fission products $^{96}_{40}$Zr is observed with the highest excitation energy (up to 4390 keV) whereas $^{134}_{43}$I has the lowest excitation energy (up to 645 keV). Moreover, the 1^+ ground state of $^{100}_{41}$Nb has the shortest half life (1.5 s) while $^{134}_{54}$Xe has the longest half life (5.8 $\times 10^{22}$y). Beta decay of the A = 100 ($^{100}_{40}$Zr - $^{100}_{41}$Nb - $^{100}_{42}$Mo) chain has been studied and $^{100}_{42}$Mo is found to have been populated via β^- decay from both the isomeric state and the ground state of $^{100}_{41}$Nb. The relative activities of the isomeric state (B) and the ground state (C) of $^{100}_{41}$Nb when both the isomeric state and the ground state β^- decay to $^{100}_{42}$Mo, have been obtained in Section 5.3.2 (the meaning of B and C is defined in Equation 5.12). Moreover, we have studied the variation of the relative intensity as a function of time of six transitions in $^{100}_{42}$Mo. A very good agreement has been observed between the variation against time of the predicted activities of the isomeric state and ground state in $^{100}_{41}$Nb and the variation against time of the intensity profiles of the 159-, 528-, 600-, 768-, 928- and 1502-keV γ-ray lines in $^{100}_{42}$Mo. It seems there is a possibility of

assigning a (4^-, 5^-) to the isomeric level in $^{100}_{41}$Nb.

In this work we have also observed the A = 134 ($^{134}_{52}$Te - $^{134}_{53}$I - $^{134}_{54}$) chain. Therefore β decay of this chain can be studied in future.

References

[1] R. E. Marrs *et al. Physics Res. A* ***592****, 463-471 (2008).*

[2] http://eprints.gla.ac.uk/58978. *October, 1997.*

[3] G. Lhersonneau *et al. Eur.Phys. Res. A* ***698****, 224-233 (2013).*

[4] G. Menzen, K. Sistemich, H. Gietz, and G. Lhersonneau. *Z. Phys. A-Atomic Nuclei* ***327****,119-126 (1987).*

[5] B. Singh. *NDS* ***81****, 1 (1997).*

[6] B. R. Martin. *Nuclear and Particle Physics (Page 1).* John Wiley and Sons, New York, 2006.

[7] R. L. Sime. *Phys. perspect.* ***2****, 48–62 (2000).*

[8] O. Hahn and F. Strassmann. *Naturwissenschaft.* ***27****, 11 (1939).*

[9] L. Meitner and O. R. Frisch. *Nature (London).* ***143****, 239 (1939).*

[10] S. J. Rose. *Minimization of actinide waste by multirecycling of thoriated fuels in an EPR.* Masters thesis, University of Oslo, Norway, 2009.

[11] D. G. Roux and E. G. Lawrie. *Lecture notes, (pages 31-33).* Rhodes University, 2013.

[12] K. S. Krane. *Introductory Nuclear Physics (Pages 160-173, 289, 292-295)*. John Wiley and Sons, New York, 1988.

[13] S. Rinta-Antila. *Development of trap-assisted spectroscopy and its application to beta decay of neutron-rich zirconium isotopes*. PhD thesis, Jyváskylá, Finland, 2006.

[14] J. M. Eisenberg and W. Greiner. *Nuclear Theory, 3rd rev. ed. (North-Holland, Amsterdam) Vol. **1***. 1987.

[15] A. D. Yamamoto. *High spin structures of transitional nuclei around the mass 100*. PhD thesis, University of Surrey, Guildford, 1994.

[16] J. N. Wilson. *A Study of Superdeformation in the Nucleus ^{133}Pr*. PhD thesis, University of Liverpool, London, 2004.

[17] http://ie.lbl.gov/toipdf/nilsson.pdf.

[18] S. Liu. *Nuclear structure studies of neutron-rich nuclei produced in the spontaneous fission of ^{252}Cf: Triaxiality near A = 110; Spherical shapes and octopole correlations beyond ^{132}Sn*. PhD thesis,Vanderbilt University, Nashville, Tennessee, 2010.

[19] X. Merita. *New gamma-ray spectrometry methods for estimating K, U,Th concentrations in rocks of Sardinia Batholith*. PhD thesis,University of Sassari, Italy, 2013.

[20] www.lanl.gov/orgs/n/n1/panda/00326397.pdf.

[21] J. E. Parks. *Compton Scattering and Gamma Ray Spectroscopy Notes, (page 8)*. The University of Tennessee Knoxville, Tennessee, 2014.

[22] T. Hinners. *Beta decay studies of neutron-rich $^{30,31}Al$ and in-beam studies of neutron-rich ^{30}Al*. PhD thesis, Florida State University, USA, 2008.

[23] A. Aguilar. *High-Spin Nuclear Structure of* ^{168,170}*Ta and Triaxial Strongly Deformed Structure in* ^{160}*Yb.* PhD thesis, Florida State University, USA, 2008.

[24] M. Guttormsen *et al. Nucl. Instr. and Meth. in Phys. Res. A* ***374****, 371-376 (1996).*

[25] arxiv.org/pdf/1306.4110.pdf.

[26] D. C. Radford. *Nucl. Instr. and Meth. in Phys. Res. A* ***361****, 297–305 (1995).*

[27] T. Rzaca-Urban *et al. Phys. Rev. C* ***79****, 024319 (2009).*

[28] D. Pantelica *et al. Phys. Rev. C* ***72****, 024304 (2005).*

[29] W. Urban. *Nucl. Phys. A* ***689****, 605–630 (2001).*

[30] S. R. Antila *et al. Eur. Phys. J. A* ***31****, 1-7 (2007).*

[31] H. Hua *et al. Phys. Rev. C* ***69****, 014317 (2004).*

[32] A. Guessous *et al. Phys. Rev. C* ***53****, 3 (1996).*

[33] S. Mukhopadhyay *et al. Phys. Rev. C* ***85****, 064321 (2012).*

[34] P. J. Daly *et al. Phys. Rev. C* ***59****, 6 (1999).*

[35] W. F. Mueller *et al. Phys. Rev. C* ***73****, 014316 (2006).*

[36] M. G. Procter. *High-K states and critical-point symmetries in* ^{138}*Gd.* PhD thesis, University of Manchester, UK, 2012.

[37] http://www.nndc.bnl.gov. *October, 2011.*

[38] B. Singh. *NDS* ***109****, 297-516 (2008).*

[39] Y. Singh *et al. Proceedings of the DAE Symp.on Nucl. Phys. , 58 (2013).*

[40] B. Kumar *et al.* *WSPC/INSTRUCTION FILE, 0:22 (2014).*

[41] www.iaea.org/newscenter/news/pioneering-nuclear-science-discovery-nuclear fission.

Appendices

Appendix A

Discovery of neutron-induced fission

Figure A.1: The apparatus used by Otto Hahn and Fritz Strassmann for the discovery of neutron-induced fission of uranium in 1938 [41].

Appendix B

The relative-intensities of γ-ray lines in $^{100}_{42}$Mo

Table B.1: The relative intensity for the 159-keV γ-ray line, gated at 536 keV. The error was obtained from the Radware fitting procedures for gamma-ray intensity. The value of the relative intensity has an arbitrary unit(a.u).

Time(s)	Relative intensity(a.u)	Error
2	808	32
4	1013	34
6	954	33
8	943	33
10	881	32
12	752	30
14	542	26
16	464	24
18	424	24
20	308	21
22	287	20
24	203	18

Table B.2: The relative intensity of the 528-keV γ-ray line, gated at 536 keV. The error was obtained from the Radware fitting procedures for gamma-ray intensity. The value of the relative intensity has an arbitrary unit(a.u).

Time(s)	Relative intensity(a.u)	Error
2	2047	41
4	2229	37
6	2310	37
8	2155	36
10	1914	34
12	1553	31
14	1327	29
16	1098	27
18	982	26
20	720	23
22	669	23
24	482	20

Table B.3: The relative intensity of the 600-keV γ-ray line, gated at 536 keV. The error was obtained from the Radware fitting procedures for gamma-ray intensity. The value of the relative intensity has an arbitrary unit(a.u).

Time(s)	Relative intensity(a.u)	Error
2	928	34
4	640	22
6	479	20
8	453	19
10	302	17
12	204	16
14	166	15
16	160	14
18	87	15
20	104	16
22	36	12
24	51	11

Table B.4: The relative intensity of the 768-keV γ-ray line, gated at 536 keV. The error was obtained from the Radware fitting procedures for gamma-ray intensity. The value of the relative intensity has an arbitrary unit(a.u).

Time(s)	Relative intensity(a.u)	Error
2	803	23
4	1172	25
6	1214	25
8	1067	24
10	881	22
12	792	21
14	511	19
16	544	20
18	417	17
20	303	16
22	275	15
24	161	14

Table B.5: The relative intensity of the 928-keV γ-ray line, gated at 536 keV. The error was obtained from the Radware fitting procedures for gamma-ray intensity. The value of the relative intensity has an arbitrary unit(a.u).

Time(s)	Relative intensity(a.u)	Error
2	697	22
4	889	23
6	883	23
8	764	21
10	706	21
12	500	19
14	544	19
16	436	18
18	336	17
20	236	15
22	228	16
24	181	14

Table B.6: The relative intensity of the 1502-keV γ-ray line, gated at 536 keV. The error was obtained from the Radware fitting procedures for gamma-ray intensity. The value of the relative intensity has an arbitrary unit(a.u).

Time(s)	Relative intensity (a.u)	Error
2	557	18
4	814	22
6	961	22
8	754	20
10	714	20
12	718	20
14	511	17
16	432	17
18	393	17
20	318	16
22	293	16
24	154	12

Appendix C

Activity

The Bateman's equations for the activity of the nth member of a chain. The prime on the lower product indicates that the $n = m$ term should be omitted.

$$\mathscr{A}_n = N_0 \sum_{t=1}^{n} c_t e^{-\lambda_t t} \tag{C.1}$$

$$= N_0 \left(c_1 e^{-\lambda_1 t} + c_2 e^{-\lambda_2 t} + ... + c_m e^{-\lambda_m t} \right) \tag{C.2}$$

$$c_m = \frac{\prod_{t=1}^{n} \lambda_t}{\prod \prime_{t=1}^{n} (\lambda_1 - \lambda_m)} \tag{C.3}$$

$$= \frac{\lambda_1 \lambda_2 \lambda_3 ... \lambda n}{(\lambda_1 - \lambda_m)(\lambda_2 - \lambda_m)(\lambda_n - \lambda_m)} \tag{C.4}$$

Table C.1: Variation of the calculated activity of Ground State(GS) and Isomeric State(IS) in $^{100}_{41}$Nb as a function of time. The calculated value of the activity has an arbitrary unit(a.u).

Time(s)	GS activity (a.u.)	Time(s)	IS activity (a.u.)	Time(s)	Avg activity (a.u.)
1	342	1	192	1	246
2	527	2	327	2	405
3	614	3	417	3	500
4	643	4	474	4	551
5	637	5	506	5	571
6	612	6	519	6	571
7	576	7	519	7	556
8	536	8	508	8	533
9	495	9	491	9	504
10	454	10	469	10	473
11	415	11	445	11	440
12	379	12	418	12	407
13	343	13	391	13	375
14	315	14	364	14	345
15	285	15	338	15	316
16	259	16	312	16	289
17	235	17	288	17	264
18	213	18	265	18	241
19	193	19	243	19	219
20	176	20	223	20	200
21	159	21	204	21	182
22	144	22	187	22	165
23	131	23	170	23	150
24	119	24	155	24	136
25	108	25	142	25	124